

ScholarWorks@GSU

Determining the Effects of Hydrothermal Alteration on the Sorption of Neptunium and Europium onto Bentonites

Authors	Kwong-Moses, Dominique S.
Citation	Kwong-Moses, Dominique S. Determining the Effects of Hydrothermal Alteration on the Sorption of Neptunium and Europium onto Bentonites. Dec. 2020, Georgia State University. https://doi.org/10.57709/19105525 .
DOI	https://doi.org/10.57709/19105525
Download date	2026-06-06 20:33:15
Link to Item	https://hdl.handle.net/20.500.14694/6349

DETERMINING THE EFFECTS OF HYDROTHERMAL ALTERATION ON THE
SORPTION OF NEPTUNIUM AND EUROPIUM ONTO BENTONITES

by

DOMINIQUE SALOMÉ KWONG-MOSES

Under the Direction of W. Crawford Elliott, Ph.D.

ABSTRACT

The Clay Mineral Society SWy-2 Na-montmorillonite clay was reacted for 90 days with 15 mM K⁺ at 200°C, the temperature/solution conditions of deep geologic repository near-field regions. X-ray diffraction of alteration products indicated that a minor amount of interstratification occurred in the clay. Hydrothermally altered samples sorbed stable Eu and ²³⁷Np almost as effectively as the unaltered clay. Average K_d values were 1.79×10^2 kg/L – 2.37×10^5 kg/L (Eu onto altered clay), 3.05×10^2 kg/L – 1.54×10^6 kg/L (²³⁷Np onto altered clay), 3.55×10^4 kg/L – 1.30×10^6 kg/L (Eu onto unaltered clay), and 1.04×10^3 kg/L (²³⁷Np onto unaltered clay). Speciation models indicated that Eu(III) and Np(V) complexation was influenced by the presence of chloride and hydroxide, but the largest observed impact on Eu and Np(V) sorption was solution pH which altered the affinity of Eu and Np(V) for the mineral surface.

INDEX WORDS: Bentonite, Deep geologic repositories, Engineered barrier systems, Neptunium, Europium, Hydrothermal Alteration, Sorption

DETERMINING THE EFFECTS OF HYDROTHERMAL ALTERATION ON THE
SORPTION OF NEPTUNIUM AND EUROPIUM ONTO BENTONITES

by

DOMINIQUE SALOMÉ KWONG-MOSES

A Thesis Submitted in Partial Fulfillment of the Requirements for the Degree of

Master of Science

in the College of Arts and Sciences

Georgia State University

2020

Copyright by
Dominique Salomé Kwong-Moses
2020

DETERMINING THE EFFECTS OF HYDROTHERMAL ALTERATION ON THE
SORPTION OF NEPTUNIUM AND EUROPIUM ONTO BENTONITES

by

DOMINIQUE SALOMÉ KWONG-MOSES

Committee Chair: W. Crawford Elliott

Committee: Brian A. Powell

Daniel M. Deocampo

Hassan A. Babaie

Electronic Version Approved:

Office of Graduate Studies

College of Arts and Sciences

Georgia State University

December 2020

DEDICATION

This thesis is dedicated to my loving parents—my mom, who has my back from across an entire ocean, and my dad, who would give us the world if he could. To my sister, Danie, and each one of my sentences that she finishes. To my Aunty Tricia who always cheers me on from the sidelines. To Alex and his level-headedness and encouragement that is so freely given. To family friends like Wiley and Joe who are there to catch me should I fall. To all my friends who congregate in the moonlight on Dutch Valley Road to share experience, strength, and hope. To my fellow Geosciences graduate students and all the times that we've come together to preserve our collective sanity. To Dr. G, for his insistence upon "COFFEE?!". To Dr. E, who has been pivotal in my development as a geoscientist ever since I wandered into his office some four years ago. To Jackson and Kyra for taking care of him, and to Ginkgo for keeping me grounded through the last leg of this process.

ACKNOWLEDGEMENTS

This thesis would have been impossible if not for some truly wonderful people—Dr. W. Crawford Elliott (“Dr. E”) and Dr. Brian A. Powell (or simply, “Brian”), my long-standing advisors and committee members. In particular, the X-ray diffraction analyses included in this study would not have been possible without the help of Dr. Daniel Gebregorgis-Yirgaw (“Dr. G”).

Data collection for this thesis coincided with the COVID-19 pandemic. Universities including Georgia State University and Clemson University opted to close their campuses, including their laboratories. These closures hindered the collection of mineralogical data that would have been obtained via X-ray diffraction, and chemical data that would have been obtained via ICP-MS.

A note of gratitude is given to the readers of this study—Dr. W. Crawford Elliott, Dr. Daniel M. Deocampo, Dr. Hassan A. Babaie, and Dr. Brian A. Powell.

A special thanks goes out to Georgia State University’s Department of Geosciences for providing the assistantship that has funded this research. The PANalytical X-ray diffractometer was purchased from funds awarded to Drs. Daniel M. Deocampo and Elliott from the National Science Foundation (Award 1029020).

Finally, this material is based upon work supported by the U.S. Department of Energy Office of Science, Office of Basic Energy Sciences and Office of Biological and Environmental Research under Award Number DE-SC-00012530.

TABLE OF CONTENTS

ACKNOWLEDGEMENTS	V
LIST OF TABLES	X
LIST OF ABBREVIATIONS	XIV
1 INTRODUCTION	1
1.1 Brief Overview of Long-Term Nuclear Waste Storage and Disposal	1
<i>1.1.1 Introduction to Generalized Geologic Repository Design</i>	<i>1</i>
<i>1.1.2 The Nature of Backfill Material</i>	<i>4</i>
<i>1.1.3 Bentonite as a Backfill Material</i>	<i>5</i>
<i>1.1.4 Hydrothermal Stability of Smectite and the Smectite → Illite Transformation</i>	<i>7</i>
<i>1.1.5 Hydrothermal Aging of Bentonite under Hypothesized Nuclear Repository Conditions</i>	<i>9</i>
<i>1.1.6 Modeling the Smectite → Illite Transformation</i>	<i>10</i>
<i>1.1.7 Composition of High-Level Nuclear Waste and Risk-Driving Constituents</i>	<i>10</i>
1.2 Purpose of this Study	19
1.3 Comprehensive Hypotheses	20
<i>1.3.1 Null Hypothesis</i>	<i>20</i>
<i>1.3.2 Hypothesis 1</i>	<i>20</i>
<i>1.3.3 Hypothesis 2</i>	<i>20</i>
<i>1.3.4 Hypothesis 3</i>	<i>20</i>

2	METHODS	21
2.1	Hydrothermal Alteration of CMS SWy-2 Na-montmorillonite.....	21
2.1.1	<i>Recovery of Hydrothermal Alteration Products</i>	<i>22</i>
2.1.2	<i>X-ray Diffraction of Hydrothermal Alteration Products</i>	<i>22</i>
2.1.3	<i>Assessment of Possible Goniometer Misalignment.....</i>	<i>22</i>
2.1.1	<i>Percentage of Illite Layers in I/S.....</i>	<i>25</i>
2.1.2	<i>001 Peak Asymmetry</i>	<i>31</i>
2.2	Batch Sorption Experiments	33
2.2.1	<i>Analysis of Quadrupole ICP-MS Data for [Np] and [Eu].....</i>	<i>34</i>
2.3	Kinetic Modeling of the Smectite → Illite Transformation	36
2.4	Speciation Modeling of Np(V), Am(III), and Eu(III) in Hydrothermal Alteration Experiments and Batch Sorption Solutions.....	37
3	RESULTS	38
3.1	Hydrothermal Alteration Experiment	38
3.1.1	<i>Extent of Interstratification in SWy-2 Na-montmorillonite</i>	<i>38</i>
3.1.2	<i>Differential 2θ ($^{\circ}$$\Delta\theta$) Values for 001/002 and 002/003 Reflections.....</i>	<i>42</i>
3.2	Batch Sorption Experiments	43
3.2.1	<i>Sorption of Neptunium onto Hydrothermal Alteration Products and Unaltered SWy-2 Na-montmorillonite</i>	<i>43</i>

3.2.2	<i>Sorption of Europium onto Hydrothermal Alteration Products and Unaltered SWy-2 Na-montmorillonite</i>	45
3.3	Kinetic Modeling of the Smectite → Illite Transformation	46
3.4	Speciation Modeling of Am(III), Eu(III) and Np(V) in Batch Sorption Solutions 	47
4	DISCUSSION	50
4.1	Hydrothermal Alteration Experiments.....	50
4.1.1	<i>Possible Solution Loss from Hydrothermal Alteration Cells via Evaporation</i>	50
4.1.2	<i>Inconsistencies in X-ray Diffraction Patterns.....</i>	51
4.1.3	<i>Semi-Quantitative Results from X-ray Diffraction</i>	52
4.1.4	<i>Qualitative Results from X-ray Diffraction.....</i>	53
4.2	Batch Sorption Experiments	53
4.2.1	<i>Sorption of Neptunium onto Hydrothermal Alteration Products and Unaltered SWy-2 Na-montmorillonite</i>	53
4.2.2	<i>Sorption of Europium onto Hydrothermal Alteration Products and Unaltered SWy-2 Na-montmorillonite</i>	54
4.3	Kinetic Modeling of the Smectite → Illite Transformation and Comparison Against Results of the Hydrothermal Alteration Experiment	55
4.4	Speciation Modeling of Am(III), Eu(III), and Np in Batch Sorption Solutions ...	56
5	CONCLUSIONS	58
	REFERENCES.....	60

APPENDICES	68
Appendix A	68
<i>Appendix A.1 X-ray Diffraction Data for Hydrothermal Alteration Experiments</i>	<i>68</i>
Appendix B	69
<i>Appendix B.1 Sorption of Np onto Hydrothermal Alteration Products and Unaltered</i>	
<i>SWy-2 Na-montmorillonite</i>	<i>69</i>
<i>Appendix B.2 Sorption of Eu onto Hydrothermal Alteration Products and Unaltered</i>	
<i>SWy-Na montmorillonite</i>	<i>72</i>

LIST OF TABLES

Table 1.1 Excerpt of Radionuclide Inventory of Spent PWR Fuel with Burn-up of 33,000 MWd/MTiHM, in Ci/MTiHM (Uranium and transuranics only; Oversby, 1986).	11
Table 1.2 Performance Objective for Control of Release Rates for Individual Radionuclides, Based on One Part in 100,000 of Their Own Inventory or 0.1% of the Calculated Release Rate Limit, Whichever is Greater (Oversby, 1986).	12
Table 2.1 Cell Matrix for Hydrothermal Alteration Experiments	21
Table 2.2 Comparison of d-Spacings and Peak Positions of a Measured Quartz Standard “Quartz Standard_02102020” and a Reference Standard “Spruce Claim Quartz Standard (RRUFF)”.	23
Table 2.3 The Positions ($\text{CuK}\alpha$) of Useful Reflections for Estimating Percent Illite in Illite/EG-smectite (Moore and Reynolds, 1997)	26
Table 2.4 Matrix for Construction of Batch Sorption Cells.....	33
Table 2.5 Solution Parameters for Speciation Modeling of Np, Am and Eu via PHREEQC	37
Table 3.1 Calculated Differential 2Θ ($^{\circ}\Delta\Theta$) Values for Experimental 001/002 with 002/003 Reflections & 17\AA Saddle/Peak Intensity Ratios with Corresponding Percent Composition of Illite Layers.	43
Table 3.2 K_d Values for Sorption of Np onto Hydrothermal Alteration Products and Unaltered SWy-2 Na-montmorillonite	44
Table 3.3 K_d Values for Sorption of Eu onto Hydrothermal Alteration Products and Unaltered SWy-2 Na-montmorillonite	45
Table 4.1 pH Measurements of Individual Batch Sorption Cells	54

LIST OF FIGURES

Figure 1.1 Generalized Schematic of the Lateral Tunnel Approach to Nuclear Waste Disposal (Boyle and Meguid, 2015).	2
Figure 1.2 Generalized Schematic for the Deep Borehole Approach to Nuclear Waste Disposal (Winterle et al., 2011).	4
Figure 1.3 Decay Curves for Risk-Driving Isotopes of the Radionuclide Inventory of PWR Spent Fuel (Burn-up 33,000 MWd-MTiHM in Ci-MTiHM; Data from Oversby 1986). 14	14
Figure 1.4 Sorption Properties of Np(V) in 0.1 M NaCl and 1 M NaCl (Zavarin et al., 2012)... 17	17
Figure 2.1 Experimentally Determined X-ray Diffraction Pattern for SiO ₂ (Ni-filtered Cu radiation, 45 kV/40 mA).	23
Figure 2.2 Reference X-ray Diffraction Pattern for SiO ₂ (Spruce Claim, King County, Washington, USA; RRUFF Project at University of Arizona).	24
Figure 2.3 Magnification of Diagnostic Peaks in the Reference X-ray Diffraction Pattern for SiO ₂ (Spruce Claim, King County, Washington, USA; RRUFF Project at University of Arizona).	24
Figure 2.4 Differential $^{\circ}\Delta\Theta$ Values for 001/002 and 002/003 Reflections versus Percent Composition of Illite Layers (Moore and Reynolds, 1997).	27
Figure 2.5 Positions of 001/002 Mixed-Layer Peaks versus Percent Composition of Illite Layers (Moore and Reynolds, 1997).	28
Figure 2.6 Positions of 002/003 Mixed-Layer Peaks versus Percent Composition of Illite Layers (Moore and Reynolds, 1997).	28
Figure 2.7 Unpublished Plot by John Hower of the 001 Saddle/Peak Intensity Ratio v. Percent Illite Layers in I/S (Elliott, 1988).	29

Figure 2.8 Inversion of John Hower's Unpublished Plot (Percent Composition Illite Layers (I/S) v. 17 Å Saddle/Peak Intensity Ratio).....	30
Figure 2.9 Useful Features of the 001 Smectite Peak for Semi-Quantitative and Qualitative Analyses	32
Figure 3.1 Overlay of Diffraction Patterns for Ethylene Glycol-Solvated Samples (Reaction cell MKM-HA2-1, after 1 and 14 weeks of hydrothermal alteration).....	38
Figure 3.2 Magnified 17Å Peak of Ethylene Glycol-Solvated CMS SWy-2 Na-montmorillonite (Reaction Cells MKM-HA2-1-1 – MKM-HA2-1-5) after 1 Week of Hydrothermal Alteration	39
Figure 3.3 Magnified 17Å Peak of Ethylene Glycol-Solvated CMS SWy-2 Na-montmorillonite (Reaction Cells MKM-HA2-1-1 – MKM-HA2-1-5) after 14 Weeks of Hydrothermal Alteration.	40
Figure 3.4 Estimation of Percent Composition of Illite Layers Using an Inverted Plot of Hower's Unpublished Data.....	41
Figure 3.5 Kinetic Model for Illitization at 200 °C and 15 mM K ⁺ (Huang et al.'s Methods; 5-Month Reaction Period; 1-day Time Step)	46
Figure 3.6 Am(III) Speciation versus pH (Simulated 0.1 mol/kgw NaCl Solution, PHREEQC) 47	
Figure 3.7 Eu(III) Speciation versus pH (Simulated 0.1 mol/kgw NaCl Solution, PHREEQC)..	48
Figure 3.8 Neptunium(V) Speciation versus pH (Simulated 0.1 mol/kgw NaCl Solution, PHREEQC).....	49
Figure 4.1 Masses of Hydrothermal Alteration Cells for the Duration of the Alteration Period (10282019-02052020).....	50

LIST OF ABBREVIATIONS

<i>Table of Abbreviations</i>	
<i>Term</i>	<i>Abbreviation Used in this Study</i>
<i>Deep Geologic Repository</i>	DGR
<i>Smectite to Illite</i>	S→I
<i>Illite/Smectite</i>	I/S
<i>High-Level Nuclear Waste</i>	HLNW
<i>Pressurized Water Reactor</i>	PWR
<i>Light-Water Reactor</i>	LWR
<i>Fast-Breeder Reactor</i>	FBR
<i>Candu Heavy Water Reactor</i>	HWR
<i>Boiling Water Reactor</i>	BWR
<i>Nuclear Regulatory Commission (USA)</i>	NRC
<i>Environmental Protection Agency (USA)</i>	EPA
<i>Mega-Watt day</i>	MWd
<i>Metric Ton of Initial Heavy Metal</i>	MTiHM
<i>Curie</i>	Ci
<i>Frayed Edge Site</i>	FES
<i>Scanning Electron Microscopy</i>	SEM
<i>Energy-Dispersive X-ray Spectroscopy</i>	EDS
<i>Inductively Coupled Plasma Mass Spectrometry</i>	ICP-MS
<i>International Atomic Energy Agency</i>	IAEA
<i>Waste Isolation Pilot Plant</i>	WIPP
<i>Abbreviations for Chemical Elements per IUPAC Periodic Table of the Elements</i>	Am, Cl, Cs, Eu, K, Na, Np, Pu, Sr, Tc, U

1 INTRODUCTION

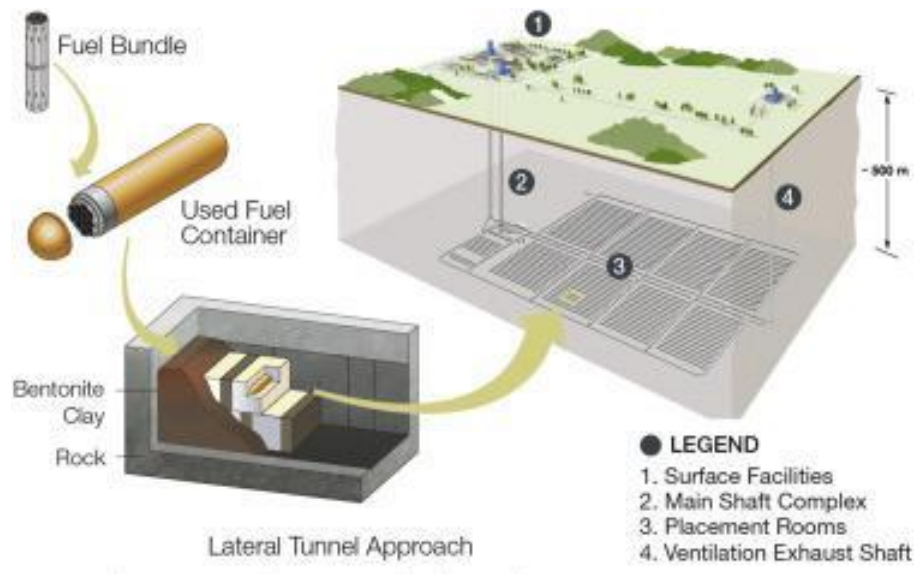
1.1 Brief Overview of Long-Term Nuclear Waste Storage and Disposal

The preferred method proposed for the long-term storage and disposal of high-level nuclear waste has been deep burial within a geologic repository (Culler, 1957; Sellin and Leupin, 2013). Deep burial geologic repositories were intended to isolate this radioactive waste from the biosphere for extended periods of time—typically 10,000 years. The release of radionuclides reaching the biosphere was projected to have been insignificant from deep the burial of high-level nuclear waste. The risk of release due to inadvertent or purposeful human activity would have been sufficiently small (Sellin and Leupin, 2013). Finally, deep geologic repositories were designed to eliminate the responsibility of future populations to maintain the repository’s physical integrity (International Atomic Energy Agency, 2009).

1.1.1 Introduction to Generalized Geologic Repository Design

The development of nuclear repository design dated back to the early 1970’s, with countries including the United States, Finland and Sweden on its forefront. There were two main approaches for long-term geologic disposal of nuclear waste that were being developed globally: the mined repository approach (*Figure 1.1*), and the deep borehole approach (*Figure 1.2*). Both approaches projected the eventual release of individual radionuclides and other elements from these fuel bundles inside the used fuel containers. In both designs, these containers were backfilled with bentonite. The proposition of bentonite as a backfill material for nuclear waste repositories came about in the late 1970’s with Swedish investigations, namely those authored by Roland Pusch, of the rock-sealing, water-uptake, and compaction properties of bentonite (Pusch, 1979; D’Appolonia Consulting Engineers, 1980).

Figure 1.1 Generalized Schematic of the Lateral Tunnel Approach to Nuclear Waste Disposal (Boyle and Meguid, 2015).



Most proposed long-term geologic repository designs were mined repositories (*Figure 1.1*), typically situated in locations with arid climates. The locations of these repositories were removed cities and large populations. In this design, tunnels, emplacement rooms, or caverns were mined from geochemically and tectonically stable geologic formations, such as salt domes, granite formations, or clay/mudstone formations. Individual waste packages were emplaced within engineered waste vessels. These vessels were placed within the open caverns—placement rooms of about 150,000 square feet each mined from surrounding bedrock, and then surrounded with backfill material (e.g. bentonite). The emplacement rooms were designed to be accessed by vertical and lateral mine shafts (Boyle and Meguid, 2015).

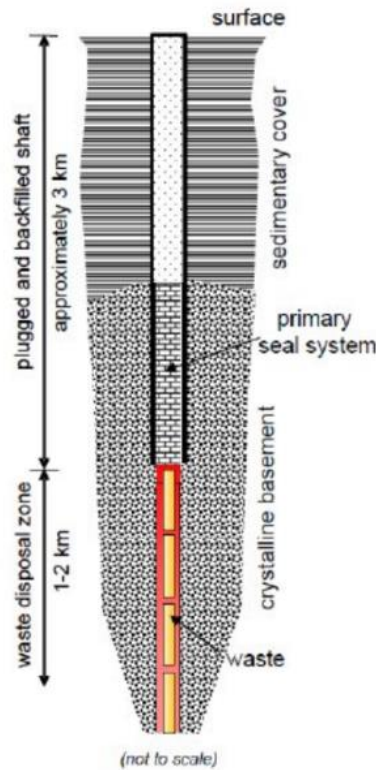
As of 2020, the United States currently operated a single nuclear waste repository via the Department of Energy (DOE) and the Nuclear Waste Partnership, LLC. This repository was of the lateral tunnel approach and was known as the Waste Isolation Pilot Plant (WIPP). The WIPP was located in the Delaware Basin salt beds 26 miles east of Carlsbad, New Mexico and the Pecos

River. The site was licensed to store transuranic waste. This site was projected to keep that waste package dry for 10,000 years. Waste vessels stored at the site were emplaced in the Salado and Castile Formation (Late Carboniferous period; 323.2-298.9 Ma) nearly half mile below the surface (Beauheim and Roberts, 2000).

Recent accidents at the Waste Isolation Pilot Plant in 2014 resulted in releases of radioisotopes including americium and plutonium. These accidents illustrated the shortcomings of the WIPP and led to questions about the site's suitability to meet the United States' nuclear disposal needs (Alvarez, 2014).

Development of a larger nuclear waste repository for the long-term storage of domestic high-level nuclear waste was approved by the United States' 107th Congress. This repository was situated within volcanic tuff at Yucca Mountain, Nevada; however, construction of the repository was incomplete and abandoned, consisting solely of an exploratory tunnel and lacking other features including emplacement rooms (Stuckless and O'Leary, 2007). The development of the Yucca Mountain repository has not fared well politically, having undergone much opposition and criticism from the local and non-local public. Sources of this opposition were widely varied—ranging from geological concerns about potential seismic activity to the site's encroachment upon land that were sacred to the native Shoshone and Paiute peoples of the southwestern United States (Fowler, 1991). Consequently, this opposition has led to dwindling and intermittent funding for research and development of the site, and as of 2010, the United States' government had withdrawn its fiscal support.

Figure 1.2 Generalized Schematic for the Deep Borehole Approach to Nuclear Waste Disposal (Winterle et al., 2011).



The second approach for long-term geologic disposal, the deep borehole approach, was designed to store waste vertically (*Figure 1.2*) in stable geologic formations such as those of interest to the lateral tunnel approach. Radioactive waste was encapsulated as waste packages. These waste packages were stored vertically in a vertical hole 5 kilometers deep. In this approach, only the bottom 2 kilometers of the borehole would contain waste; the upper 3 kilometers would be filled with backfill material (Brady et al., 2012; Winterle et al., 2011).

1.1.2 The Nature of Backfill Material

The ideal backfill material for a geologic repository shielded the surrounding environment from the eventual leakage of aqueous radionuclides (e.g. ^{90}Sr , ^{137}Cs , ^{99}Tc), and

the actinide elements (U, Np, Pu, Am). The backfill material had a relatively low hydraulic conductivity/permeability and possess self-sealing abilities. These properties were relatively constant over time (Sellin and Leupin, 2013).

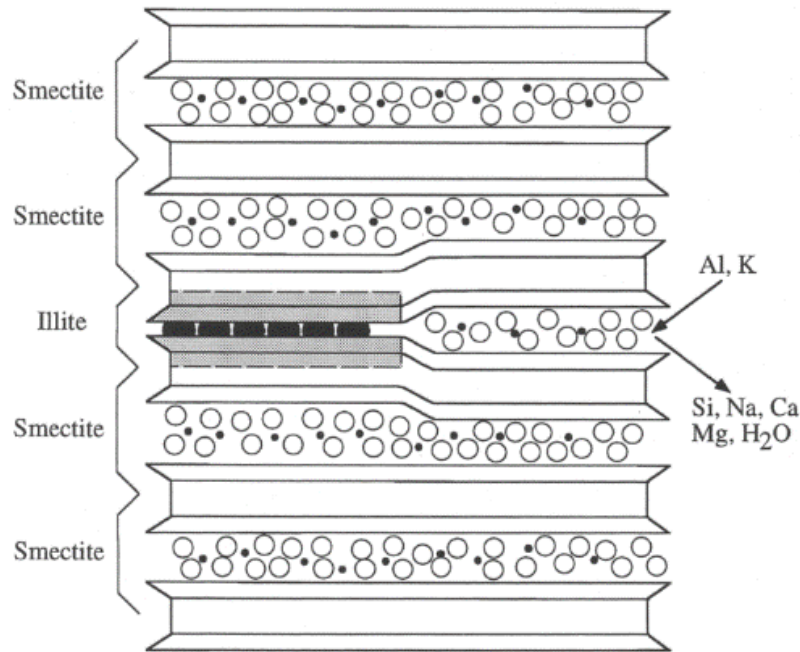
In the deep geologic repository designs, the backfill material was emplaced to sorb the released radionuclides from the individual waste vessels. The backfill material also was emplaced to seal tunnels and shafts connecting containment rooms to the surface of a nuclear repository. To date, studies that have addressed the effectiveness of bentonite as a backfill material have used test materials. These backfilled materials included: MX-80 bentonite, Jih-Hsing bentonite, GMZ bentonite, Kutch bentonite, Gaumiaozi Na-montmorillonite, Tsukinuno bentonite (Kunigel V1[®]), HDTMA bentonite, FEBEX bentonite (Ngo et al., 2014; Tsai et al., 2001; Li et al., 2016; Verma et al., 2017; Leng et al., 2016; Kozai et al., 2014; Sternik et al., 2017; Begg et al., 2015). Bentonite was to be used as a backfill material because of its low hydraulic conductivity in a saturated state (Fairhurst et al., 1996). Bentonite's low hydraulic conductivity implied that diffusion was the dominant transport mechanism in the bentonite barrier (Altaner, 1989). Bentonite was also thought to potentially control the fate and transport of radionuclides that may have leaked from waste packages (Li et al., 2016). Additionally, bentonite's swelling pressure yielded self-sealing properties that enabled it to close any gaps within the backfill mass (Sellin and Leupin, 2013).

1.1.3 Bentonite as a Backfill Material

As the proposed backfill material for high level nuclear waste repositories, bentonite will be subjected to relatively high temperatures (80° - 300°C) for extended periods of time (millions of years). When subjected to these hydrothermal conditions created by such time-temperature conditions and the presence of exchangeable alkali and alkaline earth cations (Na⁺, Ca²⁺, K⁺, Mg²⁺), the smectite within the bentonite might transform to diagenetic illite via mixed-layer illite-

smectite intermediate phases or by a dissolution/precipitation process (Figure 1.3; Moore and Reynolds, 1997; Altaner and Ylagan, 1997).

Figure 1.3 Interlayer-by-Interlayer Transformation of Smectite to Illite (Altaner and Ylagan, 1997)



Smectites, the most abundant minerals in bentonite backfill materials, have been known to possess swelling abilities, high cation exchange capacities, considerable catalytic activity and thixotropy; however, these properties were suppressed under hydrothermal treatment, as they were dependent upon the expandable nature of the clay's interlayer, which is lost upon exposure to hydrothermal treatments (Eberl et al., 1978). Zeolite, silica, or feldspar may also form depending on specific temperature and solution conditions in a process described as 'aging' (Powell, 2016; personal communication). Because the smectite \rightarrow illite transformation yielded a less-expandable phase, the resultant mixed-layer I/S clay was hypothesized to have reduced swelling pressure, sorptive properties, and self-sealing capacities than the initial starting backfill

material. The intention of this study was to characterize further the stability of smectite in bentonite under these conditions.

1.1.4 Hydrothermal Stability of Smectite and the Smectite → Illite Transformation

The smectite → illite (S → I) reaction has been explained as a function of several factors such as experimental/geologic conditions, time, temperature, including the rock-water ratio, fluid composition, redox state, and even the presence of certain microorganisms (Elliott and Matisoff, 1996; Cheshire et al., 2014, Kim et al., 2019). Additionally, the rate of S → I reaction has been accelerated due to the presence and actions of microbial organisms (Kim et al., 2004; 2019). This increased rate was accomplished via the microbial reduction of structural Fe(III) in the smectite starting material (Kim et al., 2012). At the present, however, no conclusive evidence confirmed a widespread microbially-induced S → I reaction (Kim et al., 2019).

This study focused exclusively on the abiotic formation of illite from smectite from a bentonite rock. An abiotic smectite → illite transformation has been documented to occur during burial diagenesis, regional metamorphism, hydrothermal alteration, or hydrothermal synthesis (e.g. Eberl et al., 1993). In the abiotic smectite → illite transformation, illite was created via a stepwise reaction that includes the formation of intermediate, randomly stratified and ordered mixed-layer illite-smectite intermediates at high pH. Some of these mixed-layer illite-smectite intermediates (I/S) have been interpreted as being illite solubility controlling phases and ultimately contribute to the formation of endmember illite (Yates and Rosenberg, 1996).

Mixed-layer I/S structures formed because all clay minerals can be considered as various turbostratic orderings of 2:1 layers composed of tetrahedral sheets, octahedral sheets, and interlayers cations (Eberl, 1978). The I/S intermediates were also identified via X-ray diffraction (Reynolds and Hower, 1970; Hower, 1981). The formation of mixed-layer structures followed four

general trends: the mica trend, the chlorite trend, the pyrophyllite trend, and the kaolinite trend. Each of these trends represented different reaction rates and different degrees of substitution (Eberl and Hower, 1977). The trend that was yielded from a hydrothermal alteration experiment was dependent on the identity of the interlayer cation. Alkali or alkaline earth cations yielded the mica trend, except Li-montmorillonite, which yielded the chlorite trend. Ca-montmorillonite yielded pyrophyllite and kaolinite trends at 320°C, and 150°C, respectively. A sodium-rich environment, a limited potassium supply, and the precipitation of Al-bearing minerals inhibited the S → I transformation (Cheshire et. al., 2014). The S → I transformation has been shown to follow Ostwald's step rule in some instances: the phase which involved the least change in entropy will form first, then equilibrium will gradually be approached via a stepwise reaction (Eberl and Hower, 1977).

The hydrothermal stability of illite was compared to that of muscovite over a temperature range of 100-250°C (Yates and Rosenberg, 1996). However, this comparison presented a significant void in the clay mineralogy world: the low-temperature stability of muscovite, and phase relationships between muscovite and illite were poorly defined. Illite was typically omitted from thermodynamic calculations. A known reaction sequence of muscovite → illite, illite → phengite, and finally, phengite → authigenic muscovite may have occurred over a temperature range of 185-325°C (Yates and Rosenberg, 1996).

In contrast to Yates and Rosenberg's assertion that muscovite may be used as a proxy for illite, more recent literature suggested that muscovite was unstable under the pressure, temperature and solution conditions under which authigenic illite was formed. Additionally, the recent literature suggests that illitization of clay minerals may have been influenced by maximum entropy

effects, rather than the kinetics of Ostwald ripening, per the log-normal crystallization distributions observed in clays undergoing illitization (Aja, 2019).

At high temperatures, trioctahedral smectites are more stable than dioctahedral smectites (Eberl et al., 1978). Dioctahedral smectites exhibited increased hydrothermal stability, provided that they were subjected to increased pressure, or were saturated with interlayer cations of greater hydration energy than potassium.

1.1.5 Hydrothermal Aging of Bentonite under Hypothesized Nuclear

Repository Conditions

Backfill material within a nuclear repository was expected to endure relatively high diagenetic (< 300 °C) temperatures for millions of years (Villar et al., 2012). These high temperatures occurred via different high-temperature time-temperature scenarios (Cheshire et al., 2014). One such high-temperature time-temperature scenario was approximated by a ramped temperature profile of 120-300°C for an experimental period of 3-4 weeks. An additional high-temperature scenario was approximated by an isothermal temperature profile at 300°C for six weeks (Cheshire et al., 2014). Under these hypothetical high-temperature scenarios, smectite did not convert to illite in the bentonite material (Cheshire et al., 2014). Instead, minor amounts of authigenic fibrous mineral, plagioclase, analcime, and opal-C/cristobalite were formed in the bentonite of this experiment.

It was important to note that Cheshire et al. investigated the effects of only two high-temperature scenarios, and additional high-temperature scenarios within nuclear waste repositories were also possible.

Additionally, while illitization increases with pressure from burial depth, it was assumed that the backfill material for deep geologic repositories would not experience pressures great enough to impact potential illitization.

1.1.6 Modeling the Smectite → Illite Transformation

Three models have been previously developed to describe the kinetics of the smectite → illite transformation (Elliott and Matisoff, 1996). These three models are described by Pytte, (1982); Velde and Vasseur, (1992); and Huang et al., (1993).

Briefly described, the loss of smectite (or gain in illite) was calculated in each of the three models via Arrhenius-type kinetic expressions (Elliott and Matisoff, 1996). The expressions were derived from either experimental synthesis of illite, or from iterative curve fitting to the kinetic expressions for the loss of smectite (or gain in illite) per time.

The three models did not successfully simulate the S → I transformation across a variety of geologic environments each representing a unique set of geologic ages, geothermal gradients, and potassium ion activities (Elliott and Matisoff, 1996). Hence, a new modeling approach would be needed understand the smectite → illite transformation for a nuclear repository over a geologic time period. While this research alone would be unlikely to constitute an entirely new modeling approach for the smectite → illite transformation within nuclear repository, perhaps it will contribute to the development of one such model.

1.1.7 Composition of High-Level Nuclear Waste and Risk-Driving Constituents

The inventory of radionuclides in high-level nuclear waste was typically based on the constituents of spent fuel from pressurized water reactors (PWRs), in accordance with the United States' Nuclear Regulatory Commission's performance objective (Oversby, 1986). Other varieties of nuclear reactors included light-water reactors (LWRs), fast breeder reactors (FBRs), Candu

heavy-water reactors (HWRs), and boiling water reactors (BWRs) (Rybalchenko and Colton, 1981). Each reactor type had its own characteristic burn-up rate, which described the fission energy release per unit mass of fuel as well as the temperature and isotopic composition of the irradiated fuel assemblies (Oversby, 1986; United States Nuclear Regulatory Commission, 2018). The composition of spent PWR fuel over a span of 10,000 years was calculated by Oversby (*Table 1.1*).

Table 1.1 Excerpt of Radionuclide Inventory of Spent PWR Fuel with Burn-up of 33,000 MWd/MTiHM, in Ci/MTiHM (Uranium and transuranics only; Oversby, 1986).

Table 1.1 Excerpt of Radionuclide Inventory for Spent PWR Fuel with Burn-up of 33,000 MWd/MTiHM, in Ci/MTiHM (Uranium and transuranics only; Oversby, 1986)					
<i>Nuclide</i>	Time since discharge (years)				
	10	100	300	1,000	10,000
<i>U-233</i>		1.70E-04		3.22E-03	0.048
<i>U-234</i>	1.2	1.6		2.03	1.99
<i>U-235</i>	0.02	0.02		0.02	0.02
<i>U-236</i>	0.26	0.26		0.27	0.35
<i>U-238</i>	0.318	0.318		0.318	0.318
<i>Np-237</i>	0.32	0.42		1	1.18
<i>Np-239</i>	17.1	16.9		15.6	6.7
<i>Pu-238</i>	2330	1150	237	1.08	
<i>Pu-239</i>	313	312		305	237
<i>Pu-240</i>	527	526		478	184
<i>Pu-241</i>	77600	1020	0.07		
<i>Pu-242</i>	1.76	1.76		1.72	1.69
<i>Am-241</i>	1690	3750	2750	893	
<i>Am-242</i>	7	4.6	1.9	0.1	
<i>Am-242m</i>	7	4.6	1.9	0.1	
<i>Am-243</i>	17.1	16.9		15.6	6.7
<i>Cm-242</i>	5.7	3.8	1.6	0.1	
<i>Cm-243</i>	16.6	1.86	0.01		
<i>Cm-244</i>	1320	42.1	0.02		
<i>Cm-245</i>	0.39	0.39		0.36	0.17
<i>Cm-236</i>	0.11	0.11		0.1	0.03

<i>Actinide Total</i>	83855	6854		1714	440
<i>Grand Total</i>	390855	40754		1742	465

The radionuclides listed in *Table 1.1* were considered to be “risk-driving” based on the Nuclear Regulatory Commission’s performance objective for engineered barrier systems (Oversby, 1986). This objective stipulated that “the release rate of any radionuclide from the engineered barrier system following the containment period shall not exceed one part in 100,000 per year of the inventory of that radionuclide calculated to be present at 1,000 years following permanent closure, or other such fraction of the inventory as may be approved or specified by the Commission; provided that this requirement does not apply to any radionuclide which is released at a rate less than 0.1% of the calculated total release limit. The calculated total release rate limit shall be taken to be one part in 100,000 per year of the inventory of radioactive waste, originally emplaced in the underground facility, that remains after 1,000 years of decay” (10 CFR, section 60.113 (a) (1) (ii)). In simpler terms, the release of individual radionuclides from engineered barrier systems was limited to 0.1% of their total calculated release limit by the NRC (Oversby, 1986). The inventories of radionuclides in spent PWR fuel at 1,000 years after emplacement and their respective controlled release rates were calculated by Oversby (*Table 1.2*, below).

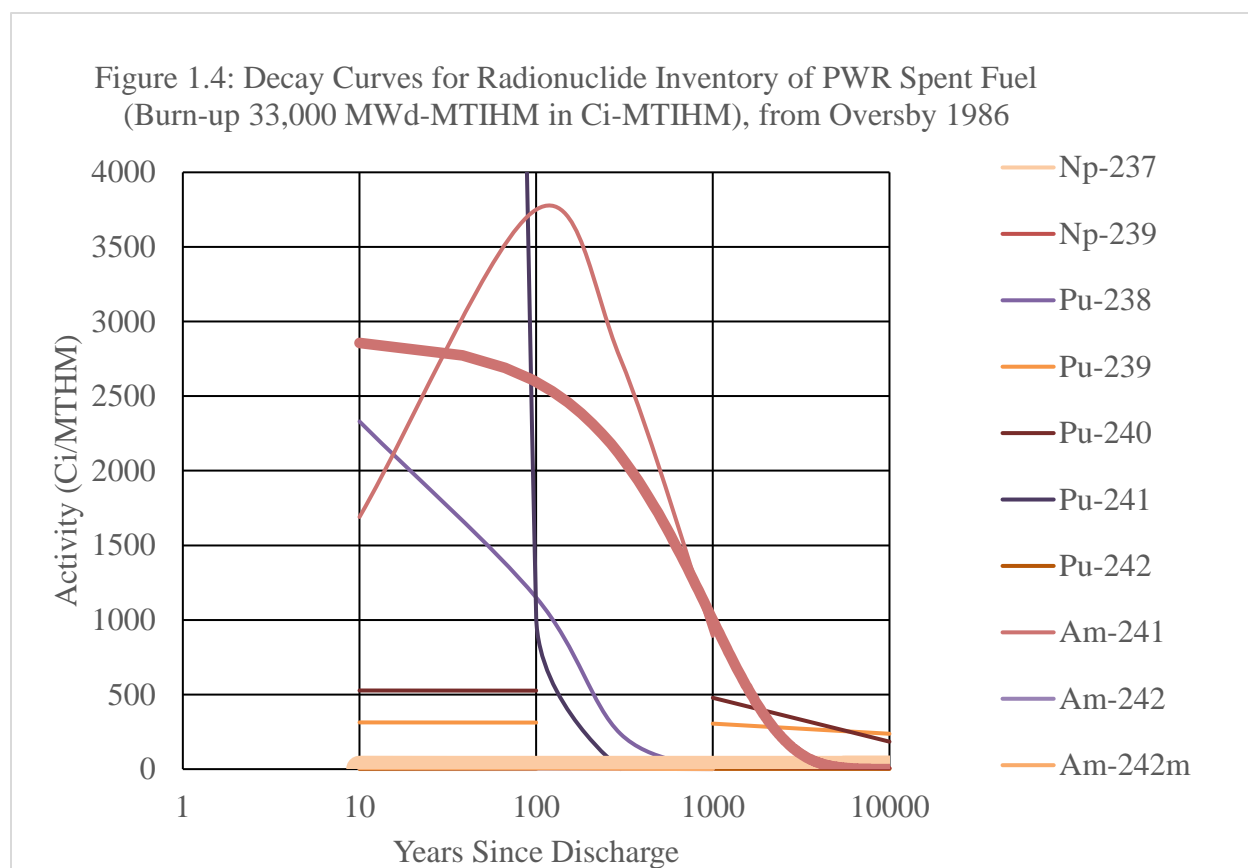
Table 1.2 Performance Objective for Control of Release Rates for Individual Radionuclides, Based on One Part in 100,000 of Their Own Inventory or 0.1% of the Calculated Release Rate Limit, Whichever is Greater (Oversby, 1986).

<p><i>Table 1.2 Performance Objective for Control of Release Rates for Individual Radionuclides, Based on One Part in 100,000 of Their Own Inventory or 0.1% of the Calculated Release Rate Limit, Whichever is Greater (Oversby, 1986)</i></p>
--

<i>Nuclide Col 1</i>	<i>Inventory at 1000y (Ci/MTHM) Col 2.</i>	<i>1/100,000 Inventory Col 3</i>	<i>Controlled Release Rate (Ci/MTHM per year)* Col 4</i>	<i>Ratio (Col 4 / Col 3)** (Col 5)</i>
<i>C-14</i>	1.38	1.38E-05	1.74E-05	1.26
<i>Ni-59</i>	5.11	5.11E-05	5.11E-05	1.00
<i>Ni-63</i>	0.38	3.8E-06	1.74E-05	4.58
<i>Se-79</i>	0.4	4.00E-06	1.74E-05	4.35
<i>Zr-93</i>	1.93	1.93E-05	1.93E-05	1.00
<i>Nb-94</i>	1.24	1.24E-05	1.74E-05	1.40
<i>Tc-99</i>	13	1.30E-04	1.30E-04	1.00
<i>Pd-107</i>	0.11	1.1E-06	1.74E-05	15.82
<i>Sn-126</i>	0.77	7.7E-06	1.74E-05	2.26
<i>I-129</i>	0.032	3.2E-07	1.74E-05	54.38
<i>Cs-135</i>	0.345	3.45E-06	1.74E-05	5.04
<i>Sm-151</i>	0.16	1.6E-06	1.74E-05	10.88
<i>Ra-226</i>	3.12E-03	3.12E-08	1.74E-05	557.69
<i>Th-230</i>	0.017	1.7E-07	1.74E-05	102.35
<i>U-233</i>	3.22E-03	3.22E-08	1.74E-05	540.37
<i>U-234</i>	2.03	2.03E-05	2.03E-05	1.00
<i>U-235</i>	0.02	2E-07	1.74E-05	87.00
<i>U-236</i>	0.27	2.7E-06	1.74E-05	6.44
<i>U-238</i>	0.318	3.18E-06	1.74E-05	5.47
<i>Np-237</i>	1	1.00E-05	1.74E-05	1.74
<i>Np-239</i>	15.6	1.56E-04	1.56E-04	1.00
<i>Pu-238</i>	1.08	1.08E-05	1.74E-05	1.61
<i>Pu-239</i>	305	3.05E-03	3.05E-03	1.00
<i>Pu-240</i>	478	4.78E-03	4.78E-03	1.00
<i>Pu-241</i>	0.02	2E-07	1.74E-05	87.00
<i>Pu-242</i>	1.72	1.72E-05	1.74E-05	1.01
<i>Am-241</i>	893	8.93E-03	8.93E-03	1.00
<i>Am-242</i>	0.1	1.00E-06	1.74E-05	17.40
<i>Am-242m</i>	0.1	1.00E-06	1.74E-05	17.40
<i>Am-243</i>	15.6	1.56E-04	1.56E-04	1.00
<i>Cm-242</i>	0.1	1.00E-06	1.74E-05	17.40
<i>Cm-245</i>	0.36	3.6E-06	1.74E-05	4.83
<i>Cm-236</i>	0.1	1.00E-06	1.74E-05	17.40
<i>* Values for 1 part in 100,000 of each radionuclide's inventory (in exponential notation).</i>				
<i>**Ratio of the values for the controlled release rate for each radionuclide (Ci/MTHM per year) to the values for 1 part in 100,000 of each radionuclides inventory (in exponential notation).</i>				

Oversby reported the release rate that the NRC allowed for each radionuclide (Column 4, *Table 1.2*). The rate listed for each species was either 0.1% of the entire inventory's release rate or 1/10,000 of the individual species' inventory. The ratio of the allowed/controlled release rate for each radionuclide to 1/10,000 of the individual species' inventory showed the relative risk (Column 5, *Table 1.2*). Isotopes with a value of unity or greater in Column 5, (wherein the controlled release rate calculated in Column 4 exceeds 1/100,000 of the radionuclide's inventory calculated in Column 3) are those that present the highest risk to contribute to the entire inventory's release rate exceeding the rate specified by the NRC. Decay curves for select risk-driving isotopes were plotted over a period of 10,000 years (*Figure 1.3*), with exponential trendlines for the decay of ^{237}Np and ^{241}Am , the two isotopes of interest to this study.

Figure 1.3 Decay Curves for Risk-Driving Isotopes of the Radionuclide Inventory of PWR Spent Fuel (Burn-up 33,000 MWd-MTiHM in Ci-MTiHM; Data from Oversby 1986).



1.1.7.1 Neptunium as a Constituent of High-Level Nuclear Waste

Based on the foregoing modeled inventories, and the inventories of its daughter products, Np is considered to be a significant contributor to the cumulative radioactivity of the radionuclide inventory of spent PWR fuel. Thus, Np was chosen to be an element of interest to this study.

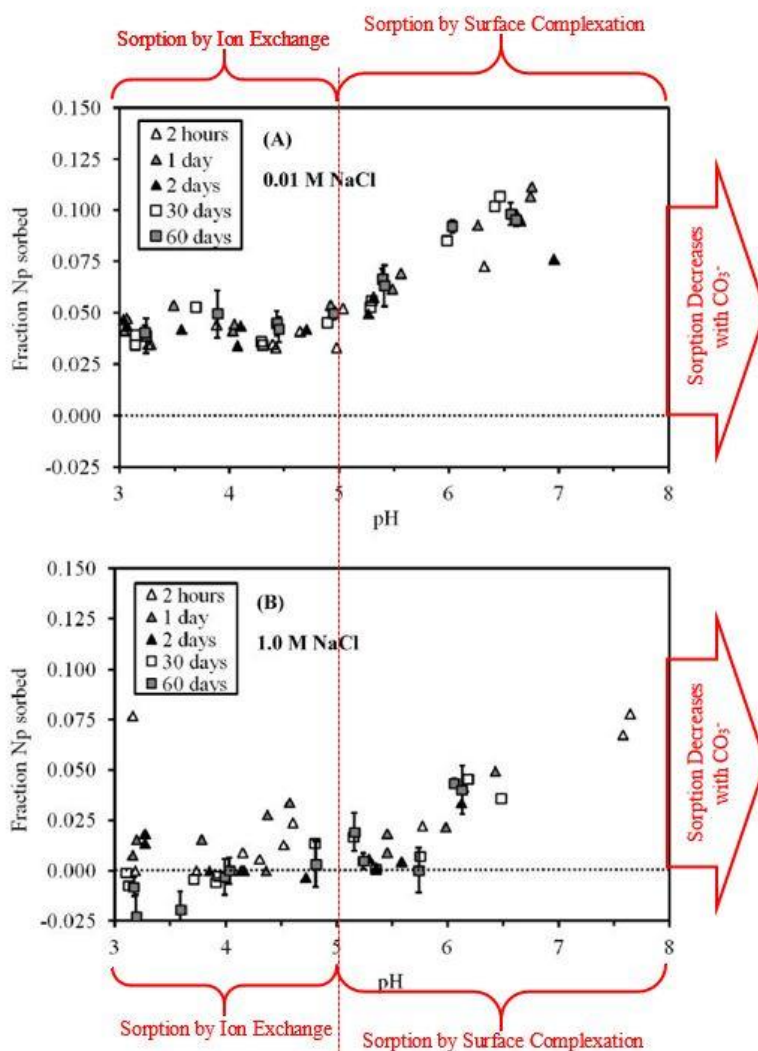
As a result of its redox potentials, the most likely oxidation states of neptunium in the environment were predicted to be Np(IV) and Np(V)—Np(IV) was formed under anoxic conditions, and Np(V) was formed under mildly oxic conditions (Zavarin et al., 2012).

In terms of Eh-pH behavior, NpO_2^+ displayed high solubility under oxidizing conditions and was hence the most prevalent Np-bearing species in natural waters (Banik et al., 2017). Banik et. al also compared Np(V) surface complexation with illite to that of Np(IV), and found that the

Np(IV) surface complex held a stronger bond with itself and illite, and was thus considerably more thermodynamically stable. Due to this increased thermodynamic stability, Np(V) was partially reduced to Np(IV) at the illite surface, which caused a strong interaction between Np and illite. Additionally, ionic strength had minimal impact on the sorption of Np(V) and Np(IV) onto illite. Np uptake was sensitive to pH and reduction potential (Banik et al., 2017).

Regarding the sorption of Np(V) onto smectites, the processes involved were found to be pH dependent. At low pH (below pH 5) sorption occurred via ion exchange. Between pH 5 and pH 8, surface complexation processes were responsible, and sorption increased with pH within this range. Above pH 8, sorption of Np(V) onto smectites decreased with the presence of carbonate (*Figure 1.5; Zavarin et al., 2012*).

Figure 1.4 Sorption Properties of Np(V) in 0.1 M NaCl and 1 M NaCl (Zavarin et al., 2012).



As a minor constituent of HLNW, ^{237}Np had a relatively long half-life (2.0×10^6 years). Combined with its complex decay paths, this long half-life brought significance to the presence of ^{237}Np in HLNW. When the long-term viability of a site was assessed, it was necessary to account for the radionuclide's slew of daughter products in terms of inventory, radiotoxicity and mobility (Ojovan et al., 2019).

At the time of disposal, any Np present in HLNW was likely to be Np(V). Np(V) had a lower surface-complexation affinity than Np(IV), due to the distribution of the neptunyl ion's overall charge between its two oxygens. This distribution gave the ion's effective charge of $\sim +2.3$. As such, $^{237}\text{Np(V)}$ was one of the most mobile radionuclides in HLNW (Pope, 2017). Combined with the various properties of its daughter products, especially in terms of radiotoxic effects, and its extreme mobility, $^{237}\text{Np(V)}$ was considered to be "risk driving", despite its minor contribution by mass to the radionuclide inventory of spent nuclear fuel.

1.1.7.2 Americium as a Constituent of High-Level Nuclear Waste

Along with Np, Am was cited as being another major element influencing the long-term radiotoxicity of nuclear waste due to its long half-life (Frohlich and Kaplan, 2018). Additionally, americium's long-lived nature made its geochemical properties particularly relevant to understanding the dissolution process of spent PWR fuel (Oversby, 1986). The present study focused on ^{241}Am .

Strongly reducing conditions created by the degradation of steel engineered waste vessels caused Am to exist primarily in its +3 oxidation state (Frohlich and Kaplan, 2018).

The mechanisms involved in the sorption of Am(III) onto 2:1 clay minerals were highly dependent upon solution pH. Sorption of Am onto minerals such as smectite and illite was governed by cation exchange at low pH. However, at high pH, sorption mechanisms onto these minerals were dominated by cation exchange processes (Frohlich and Kaplan, 2018). The reversibility of sorption of Am(III) onto smectites and illites was found to be dependent on solution pH as well. Lower solution pH resulted in the formation of outer sphere complexes on ion exchange sites which facilitated rapid exchange, thus facilitating the reversibility of the sorption

reaction. At high pH, inner sphere complex formation on ion exchange sites hindered desorption processes (Kumar et al., 2013).

1.1.7.3 The Use of Europium as a Proxy for Americium

In working with Am, it was important to consider that although Am was a strong α -emitter, many of its daughter products are γ -emitters. When working with quantities of Am on the order of grams, the intense gamma radiation from these daughter products was found to be problematic (Hobart, 2013). While the present study only required Am in much smaller quantities, its homolog, europium (Eu), was used in the place of Am—The two elements have homologous electron configurations in their ground and ionized states, but Eu is a stable element (Schulz, 1976). Additionally, because the present study relied heavily on sorption experiments, the atomic radii of the two elements was important to consider. Am has an atomic radius of 244 pm, and europium has an atomic radius of 233 pm. Am was only about 4% larger than Eu, and this difference was assumed to be negligible for the study of sorption behavior. It should be noted that stable Eu was used in this study, which was a mixture of ^{151}Eu and ^{153}Eu .

1.2 Purpose of this Study

The purpose of this study was to explore the behavior of bentonite (SWy-2 Wyoming montmorillonite) and its interactions with the risk driving radionuclides ^{237}Np and ^{241}Am under a hypothesized high-temperature scenario within a deep geologic repository. Interactions with ^{241}Am were examined via use of stable Eu. This experiment attempted to force the hydrothermal aging of smectite in a sample of SWy-2 Na-montmorillonite to simulate a high-temperature scenario within a deep geologic repository. Both hydrothermal alteration products and the unaltered SWy-2 Na-montmorillonite were introduced into solutions containing ^{237}Np and stable Eu, and to evaluate possible changes in sorption behavior induced by hydrothermal alteration. This

study was intended to build on existing literature that characterizes the viability of bentonites for application to backfill material in nuclear waste repository design.

1.3 Working Hypotheses

Considerations of this study's experimental design, wherein hydrothermal alteration experiments were followed by batch sorption experiments, yielded four working hypotheses.

1.3.1 Null Hypothesis

The hydrothermal alteration experiment will not induce the S→I transformation, and smectite is stable under these reaction conditions. Hydrothermal alteration products will be able to sorb and/or fix Np and Eu. Smectite remains to be an optimum sorbent for Np and Eu.

1.3.2 Hypothesis 1

The hydrothermal alteration experiment will induce the S→I transformation, yielding products that are interstratified and/or endmember illite. Alteration products will be less effective at sorbing Np and Eu compared to unaltered bentonite.

1.3.3 Hypothesis 2

The hydrothermal alteration experiment will not induce the S→I transformation, yielding neither interstratified I/S, nor endmember illite. However, reaction products will be unable to sorb and/or fix Np and Eu.

1.3.4 Hypothesis 3

The hydrothermal alteration experiment will create interstratified I/S or endmember illite. Reaction products will be able to sorb and/or fix Np and Eu.

2 METHODS

2.1 Hydrothermal Alteration of CMS SWy-2 Na-montmorillonite

Five reaction cells were constructed using Clay Mineral Society (CMS) SWy-2 Na-montmorillonite source clay material, solutions of 15 mM KCl, 15 mM KOH and 18 MΩ deionized water in 120 mL PTFE Savillex digestion vials (conical interior, cored exterior, buttress threaded top), per the sample matrix outlined below (*Table 2.1*). These test portions were created with an initial solid: solution ratios of 1:10 (mass: mass). Each cell was constructed with 20 g solution and approximately 2 g clay.

Table 2.1 Cell Matrix for Hydrothermal Alteration Experiments

Table 2.1: Cell Matrix for Hydrothermal Alteration Experiments		
<i>Sample ID</i>	Solution	Clay (SWy-2 Na-montmorillonite) (g)
<i>MKM-HA2-1</i>	15 mM KOH	2.04
<i>MKM-HA2-2</i>	15 mM KOH	2.04
<i>MKM-HA2-3</i>	15 mM KCl	2.04
<i>MKM-HA2-4</i>	15 mM KCl	2.03
<i>MKM-HA2-5</i>	18 MΩ DI H ₂ O	2.06

Reaction cells were heated at 200°C using a Thermolyne hot plate in a dry sand bath for approximately ninety days. The cells were sampled weekly by removing small portions (~3.0 g) of mixed solid and solution to create oriented mounts on petrographic slides for mineralogic analyses via X-ray diffraction. Over the course of the reaction period, sand and hot plate temperatures were monitored to ensure stable reaction conditions. Additionally, the reaction cells were weighed periodically to track possible solution loss by evaporation (*Table 4.1*).

2.1.1 Recovery of Hydrothermal Alteration Products

At the end of the ninety-day reaction period, hydrothermal reaction products were recovered for use in batch sorption experiments at Clemson University. To remove excess K^+ , reaction products were cleaned via dialysis with 2 M Ω DI H₂O for 48-hours with frequent changes of the deionized water. Cleaned reaction products were then dried in a laboratory oven for 12 hours at a low temperature (50°C) to protect the integrity of the clay structure. Following drying, the clay samples were crushed via mortar and pestle, and weighed.

2.1.2 X-ray Diffraction of Hydrothermal Alteration Products

Materials sampled from the hydrothermal cells were mounted on petrographic slides (23 by 46 mm) to construct oriented mounts for X-ray diffraction analyses. Three oriented mounts were created for every sample. The first mounts were air-dried. The second set of mounts were solvated with ethylene glycol vapor for 24 hours to expand the smectite interlayer, and the third set of mounts were heated at 500°C for 1 hour to collapse the smectite interlayer (Moore and Reynolds, 1997).

All mounts were scanned using a PANalytical X'Pert Pro™® X-ray diffractometer, with Cu radiation generated at 45 kV and 40 mA with a nickel filter. The mounts were scanned at roughly 1°2 θ /minute from 0-35°2 θ using ½° divergence and receiving slits.

2.1.3 Assessment of Possible Goniometer Misalignment

To assess possible goniometer misalignment, a diffraction pattern was obtained from a standard mount of SiO₂ using the same run conditions for diffraction of the hydrothermal alteration samples (*Figure 2.1*). Experimental d-spacings for SiO₂ were calculated from measured peak positions using Bragg's Law. Additionally, a reference pattern for SiO₂ was obtained from the

RRUFF Project at Arizona State University and calculated experimental d-spacings of this study were compared to those of the reference pattern for SiO₂. (Figures 2.2 and 2.3).

Figure 2.1 Experimentally Determined X-ray Diffraction Pattern for SiO₂ (Ni-filtered Cu radiation, 45 kV/40 mA).

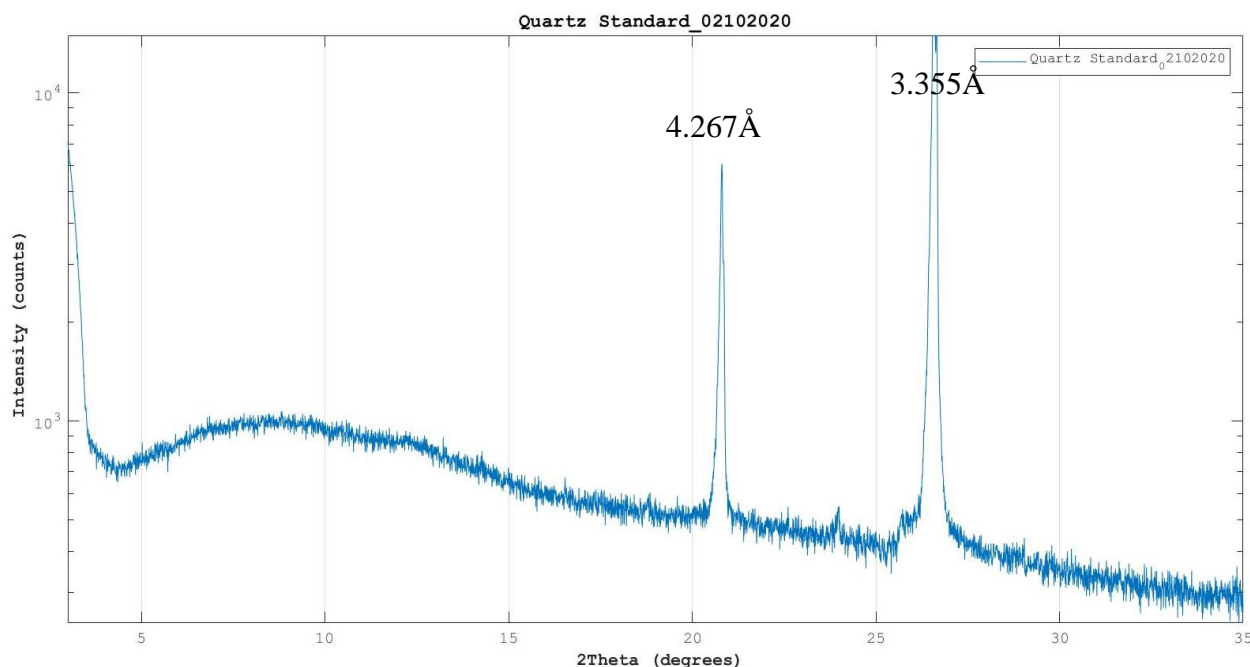
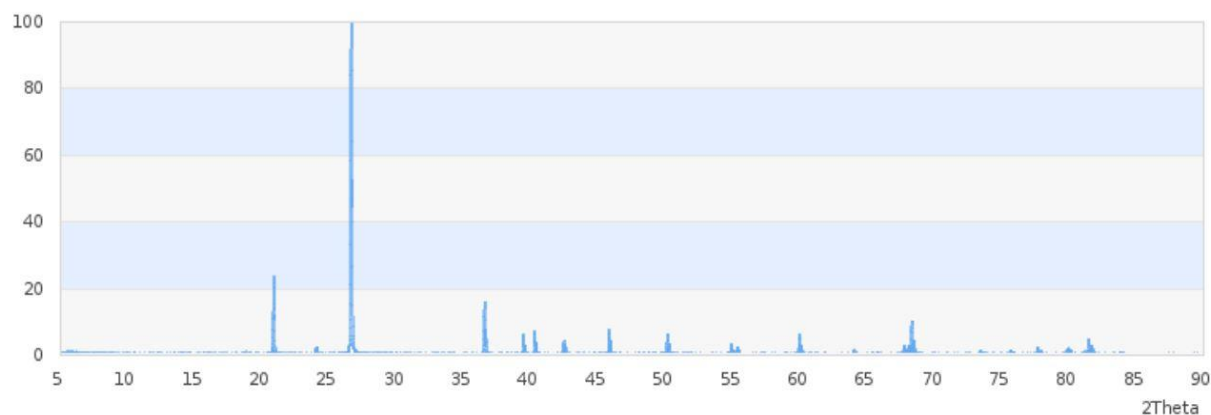


Table 2.2 Comparison of d-Spacings and Peak Positions of a Measured Quartz Standard “Quartz Standard_02102020” and a Reference Standard “Spruce Claim Quartz Standard (RRUFF)”.

Table 2.2: Comparison of d-spacings and peak positions of a measured quartz standard “Quartz Standard_02102020” and a reference standard “Spruce Claim Quartz Standard (RRUFF)”				
<i>Sample</i>	Peak 1		Peak 2	
	d-spacing (Å)	Position (°2θ)	d-spacing (Å)	Position (°2θ)
“Quartz Standard_02102020”	4.2672 Å	20.80°	3.3558 Å	26.54°
“Spruce Claim Quartz Standard (RRUFF)”	4.2626 Å	20.84°	3.3475 Å	26.63°
<i>Peak Shift</i>	0.0046 Å	0.04°	0.0083 Å	0.09°

The 4.26Å and 3.34Å peaks for the measured quartz standard (“Quartz Standard_02102020”) were shifted 0.04° and 0.09° towards the high $^{\circ}2\Theta$ side of the diffraction pattern, compared to the reference standard “Spruce Claim Quartz Standard (RRUFF)”.

Figure 2.2 Reference X-ray Diffraction Pattern for SiO₂ (Spruce Claim, King County, Washington, USA; RRUFF Project at University of Arizona).

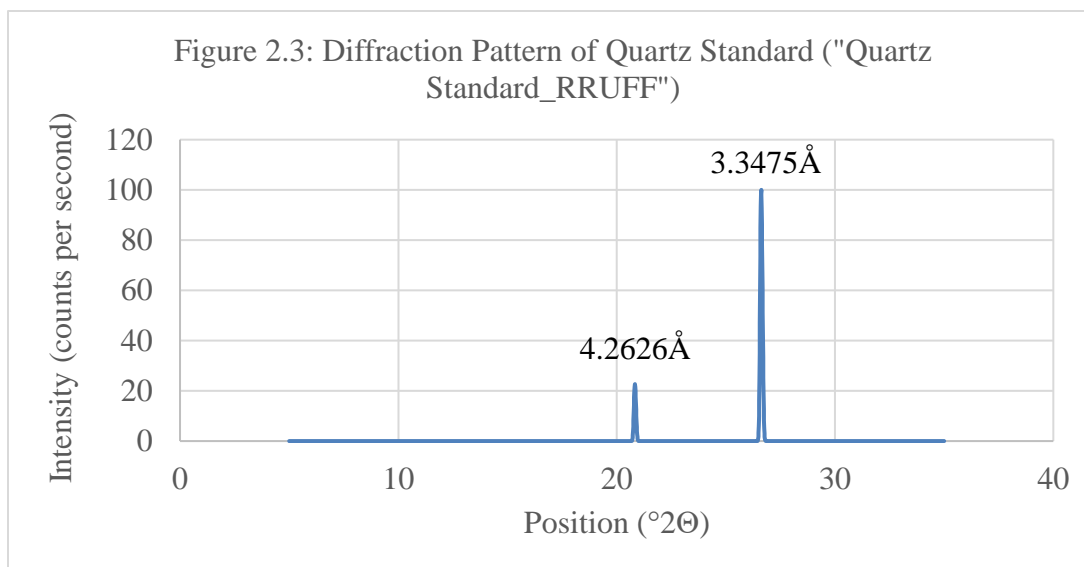


Radiation - Copper K α

Data Set: Spruce Claim, King County, Washington, USA 73

Data courtesy of RRUFF project at University of Arizona, used with permission.

Figure 2.3 Magnification of Diagnostic Peaks in the Reference X-ray Diffraction Pattern for SiO₂ (Spruce Claim, King County, Washington, USA; RRUFF Project at University of Arizona).



2.1.1 Percentage of Illite Layers in I/S

Diffraction patterns for the ethylene glycol-solvated mounts were used to determine percentage of illite layers in interstratified I/S, as these patterns were more indicative of interstratification than air-dried or heated patterns (Moore and Reynolds, 1997). Semi-quantitative mineralogical analyses of these patterns were facilitated by use of PANalytical's HighScore Plus™ Software interfaced to the X-ray diffractometer to determine the d-spacing values of the observed diffraction peaks per Bragg's Law:

$$n\lambda = 2d \sin\theta ,$$

Where λ is the wavelength of the Ni filtered Cu K α radiation, θ is the angle of diffraction, and n is the order of diffraction. The observed d-spacing values for I/S reflections were tabulated and compared against those calculated by Moore and Reynolds (1997). The positions ($^{\circ}2\theta$) of mixed-layer peaks including the 001₁₀/, 002₁₇ and 002/003₁₇ reflections were tabulated (*Table 3.1*). Differential 2θ values for the 001/002 and 002₁₀/003₁₇ reflections were calculated as:

$$^{\circ}\Delta 2\theta = 2\theta (001_{10}/002_{17}) - 2\theta (002_{10}/003_{17})$$

where $^{\circ}\Delta 2\theta$ is the difference in 2θ between the positions of the $002_{10}/003_{17}$, and $001_{10}/002_{17}$ peaks in units of $^{\circ}2\theta$. Calculations for differential 2θ values were consistent with the methods and detailed by Moore and Reynolds in 1997.

In past studies of I/S bearing samples, the positions of mixed-layer peaks and differential 2θ values were useful in estimating a sample's percent composition of illite layers. While d-spacings may also be used to estimate percentages of illite layers, differential 2θ values were insensitive to potential error caused by goniometer zero-alignment and sample displacement issues (Środoń, 1980; Moore and Reynolds, 1997). Curves of differential 2θ values and the positions of mixed-layer peaks were calculated by Moore and Reynolds (1997), and the present study plotted these values against percent composition of illite layers (*Table 2.3; Figures 2.4, 2.5 and 2.6*). The positions of mixed-layer peaks and differential 2θ values from the present study were then added to those curves to facilitate the extrapolation of percent composition of illite layers in experimental hydrothermal alteration cells (*Figure 3.5*).

Additionally, the Reichweite (R) descriptor was used to show the stacking order of the I/S layers. $R = 0$ signified a random stacking order of I (illite) and S (smectite) layers. $R \geq 1$ signified a stacking order where S is followed by I and where S is not followed by S. $R \geq 3$ signified as stacking order where S was followed by at least three I layers.

Table 2.3 The Positions (CuK α) of Useful Reflections for Estimating Percent Illite in Illite/EG-smectite (Moore and Reynolds, 1997)

Table 2.3: Moore & Reynolds, Table 8.3. The positions (CuK α) of useful reflections for estimating percent illite in illite/EG-smectite

% Illite	Reichweite	001/002		002/003		$^{\circ}\Delta 2\Theta$
		d(Å)	$^{\circ}2\Theta$	d(Å)	$^{\circ}2\Theta$	
10	0	8.58	10.31	5.61	15.8	5.49
20	0	8.67	10.2	5.58	15.88	5.68
30	0	8.77	10.09	5.53	16.03	5.94
40	0	8.89	9.95	5.50	16.11	6.16
50	0	9.05	9.77	5.44	16.29	6.52
60	1	9.22	9.59	5.34	16.6	7.01
70	1	9.4	9.41	5.28	16.79	7.38
80	1	9.64	9.17	5.2	17.05	7.88
90	3	9.82	9.01	5.10	17.35	8.38

Figure 2.4 Differential $^{\circ}\Delta 2\Theta$ Values for 001/002 and 002/003 Reflections versus Percent Composition of Illite Layers (Moore and Reynolds, 1997).

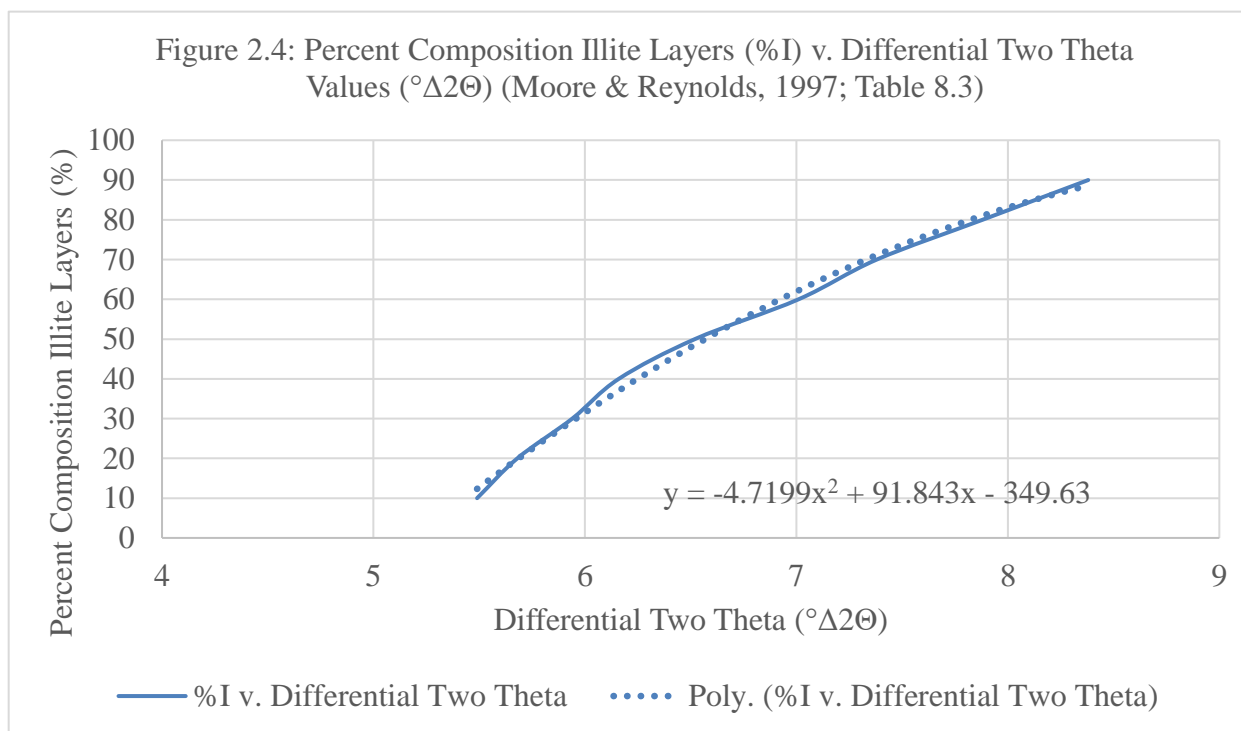


Figure 2.5 Positions of 001/002 Mixed-Layer Peaks versus Percent Composition of Illite Layers (Moore and Reynolds, 1997).

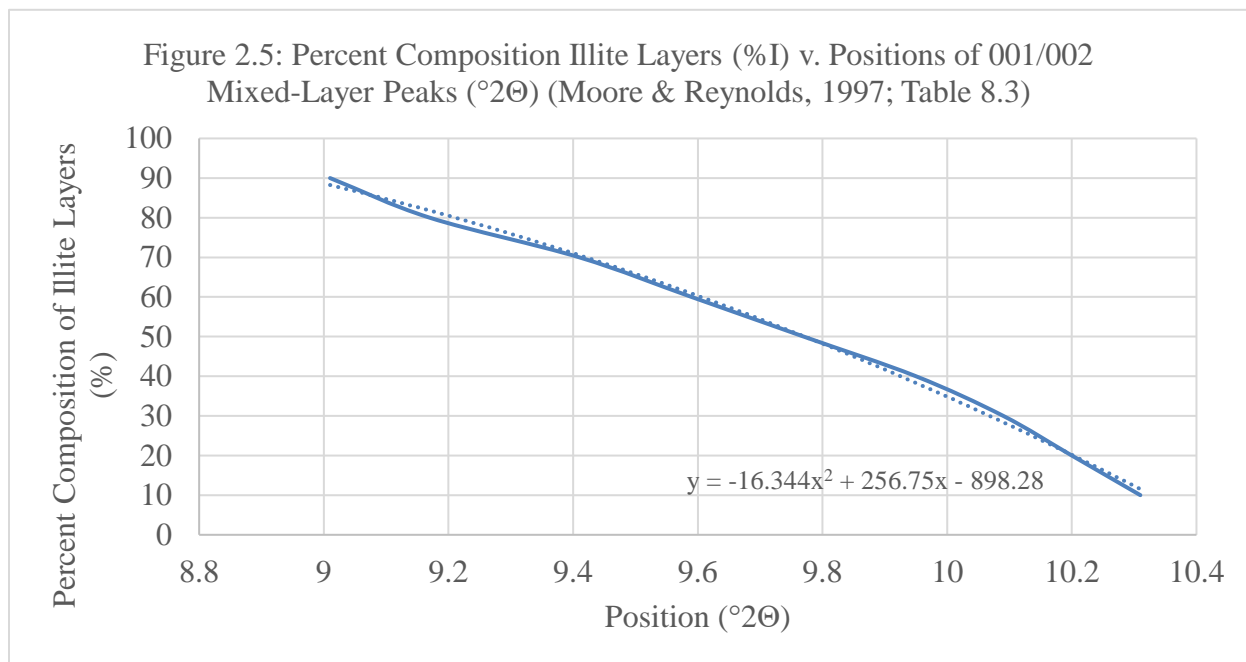
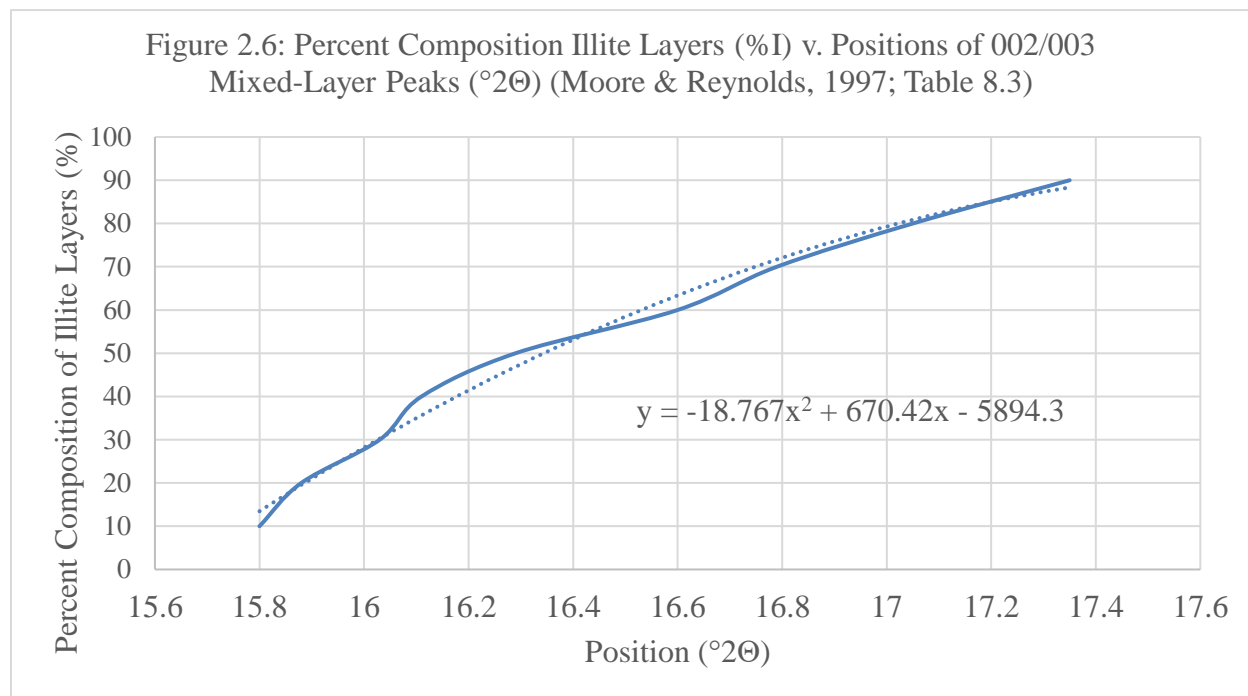


Figure 2.6 Positions of 002/003 Mixed-Layer Peaks versus Percent Composition of Illite Layers (Moore and Reynolds, 1997).



In addition to d-spacing values and differential 2Θ values for the I/S reflections, the intensities of the 001 peaks (17 \AA) were tabulated against their intensities at the “saddles” (“i”, *Figure 2.9*). The term “saddle” was coined by John Hower, referring to the minima that occurs on a diffraction pattern on the high d-spacing side of the 001 smectite peak. Hower correlated the ratios of the intensities of the “saddle” to that of the 17 \AA peak to a sample’s percent composition of illite layers (I/S; *Figure 2.7*).

Figure 2.7 Unpublished Plot by John Hower of the 001 Saddle/Peak Intensity Ratio v. Percent Illite Layers in I/S (Elliott, 1988).

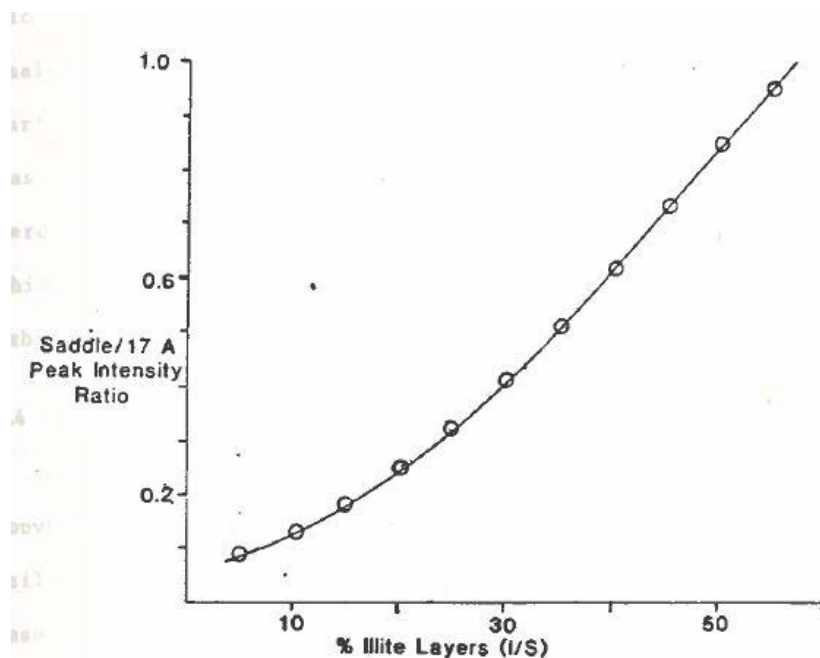
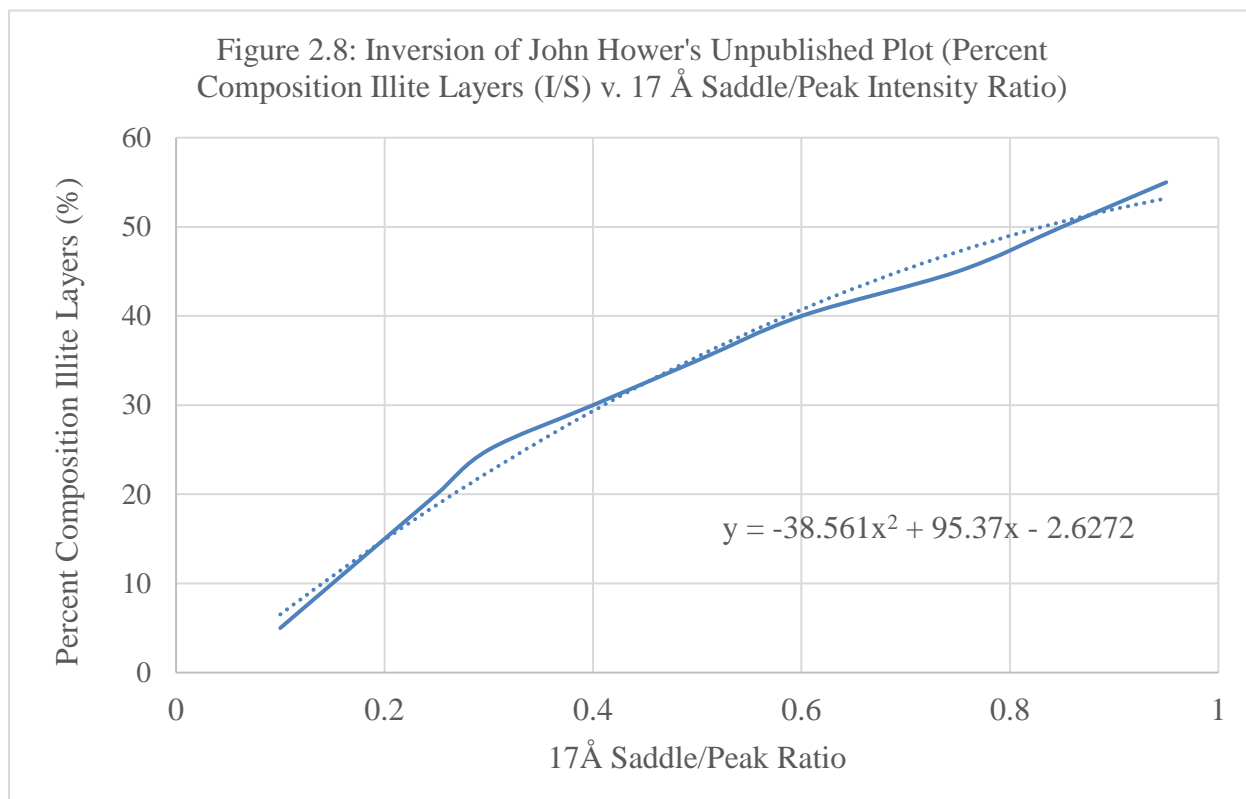


Figure 2-3: The (001)₁₇ peak/saddle ratio versus percent illite layers in I/S. Unpublished data from Hower.

For this study, Hower's unpublished plot was inverted by extrapolating x and y values from the original plot (Figure 2.8). A second-order polynomial function was generated to describe Hower's curve. This function was used to calculate values for percentage of illite layers from experimental data for the 17Å saddle/peak intensity ratios obtained from several diffraction patterns of the hydrothermal alteration experiment's montmorillonite at the beginning of the reaction period, and the end of the reaction period.

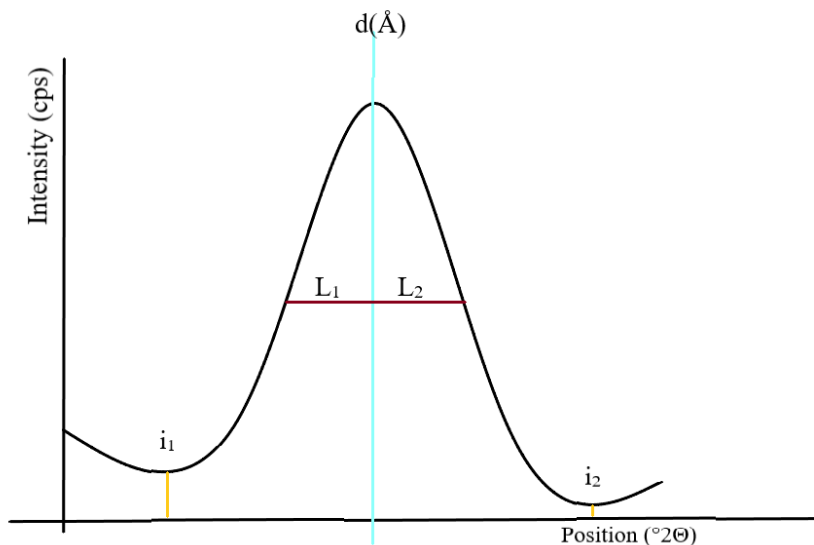
Figure 2.8 Inversion of John Hower's Unpublished Plot (Percent Composition Illite Layers (I/S) v. 17 Å Saddle/Peak Intensity Ratio)



2.1.2 001 Peak Asymmetry

Asymmetry of the 17Å peak may also be used as an indicator of interstratification or incipient interstratification in smectite-bearing samples. Ratios of the quantities “L₁” and “L₂” (Figure 2.9), were calculated and were used to verify peak asymmetry by a deviance of the L₁/L₂ from unity.

Figure 2.9 Useful Features of the 001 Smectite Peak for Semi-Quantitative and Qualitative Analyses



To date, the literature concerning the smectite to illite transformation has not quantitatively been related to a value for percent composition of illite layers to the L_1/L_2 ratio, thus this metric represents only qualitative data. However, upon examination of I/S calculated patterns, there was a trend of increasing percent composition of illite layers with increasing peak asymmetry. Likewise, the intensity of the saddle peak intensity ratio was positively correlated with increasing percent composition of I/S layers in a sample.

A final indicator of interstratification in smectite-bearing samples was the presence of small oscillations in intensity measured on the high d-spacing side of the 17\AA peak. These oscillations were far below the instruments signal to noise ratio; however, they resulted in a “jagged” appearance of peaks if examined very closely. The presence of these minute oscillations qualitatively correlated to interstratification in I/S samples. These jagged peak shapes on the high d-spacing side may also have been indicative of interstratification or incipient interstratification seen before shifts in the lower order I/S reflections.

2.2 Batch Sorption Experiments

Each of the five samples recovered from the hydrothermal alteration experiments were split into ~0.1g subsamples to create reaction cells for batch sorption experiments at Clemson University (PI: Dr. Brian A. Powell). In addition to the batch sorption cells made using the altered clay, five cells of the unaltered SWy-2 material were constructed in a similar fashion.

A total of 30 cells were constructed and split among five groups, each with different volumes of Np spikes, and equal volumes of Eu spikes. The Np spike added to each cell had a concentration of 2.0×10^{-4} M, and the Eu spike had a concentration of 6.0×10^{-5} M. Each cell's solid: solution ratio was maintained at a 1:10 mass ratio, using 10 mM NaCl as a background solution. A matrix of cells was created for the present study's batch sorption experiments (*Table 2.4*).

Table 2.4 Matrix for Construction of Batch Sorption Cells

<i>Table 2.4: Matrix for Construction of Batch Sorption Cells</i>											
<i>Cell Group</i>	<i>Sample ID</i>	<i>Clay_T (g)</i>	<i>Clay_A (g)</i>	<i>10 mM NaCl_T (mL)</i>	<i>10 mM NaCl_A (mL)</i>	<i>Np Spike_T (μL)</i>	<i>Np Spike_A (g)</i>	<i>Eu Spike_T (μL)</i>	<i>Eu Spike_A (g)</i>		
1	1-1	0.1	0.1092	9.95	9.9032	50	0.0480	50	0.0532		
	2-1 ¹										
	3-1		0.1049						9.9618	0.0480	0.0527
	4-1		0.1043						9.9286	0.0484	0.0577
	5-1		0.1046						9.9336	0.0844	0.0531
	6-1		0.1050						9.7049	0.0541	0.0544
2	1-2	0.1	0.1003	9.90	*	250	0.2428	50	0.0547		
	2-2 ¹										
	3-2		0.1009						9.8585	0.2465	0.0532
	4-2		0.1010						9.8102	0.2429	0.0527
	5-2		0.1013						9.8153	0.0948*	0.0509
	6-2		0.1037						9.7049	0.2463	0.0538
3	1-3	0.1	0.1020	9.5	9.3952	500	0.5019	50	0.0540		
	2-3 ¹										
	3-3		0.1018						9.3736	0.5043	0.0577
	4-3		0.1038						9.4040	0.5057	5.041
	5-3		0.1022						9.4615	0.5070	*
	6-3		0.1074						9.1713	0.5052	0.0542

4	1-4		0.1070	9.0	9.0323	1000	6.0282		0.0542	
	2-4 [†]									
	3-4		0.1005		8.9121		1.0052		0.0539	
	4-4		0.1023		8.8991		1.0064		0.0541	
	5-4		0.1002		8.8753		1.0060		0.0543	
	6-4		0.1169		8.7347		1.0015		0.0554	
5	1-5		0.1133	5.0	4.9692	5000	5.0063		0.0558	
	2-5 [‡]		0.0905		4.9631		4.6630		0.0575	
	3-5		0.1095		4.9777		5.0276		0.0546	
	4-5		0.1024		4.9557		5.0758		0.0568	
	5-5		0.1005		4.9675		4.9367		0.0563	
	6-5		0.1131*		4.9100		5.8957		0.0550	
<p>* Tare error</p> <p>[†] Large portion of hydrothermal alteration cell MKM-HA2-2 lost during dialysis</p> <p>[‡] One batch sorption cell was created using the remaining clay from hydrothermal alteration cell MKM-HA2-2</p>										

Hydrothermal alteration cells (*Table 2.4*) were tumbled for about 180 days, with samplings occurring approximately every 60 days.

For sampling, batch sorption cells were removed from the tumbling apparatus and each cell's pH was measured. Then, 1.3 mL of suspension was pipetted gravimetrically from each cell and placed into 2 mL centrifuge tubes. Suspension samples were centrifuged at 8000 rpm for 20 minutes, and 1 mL of the supernatant was pipetted gravimetrically from the centrifuged suspensions into 15 mL centrifuge tubes and diluted with 9.0 mL 2% HNO₃ for quadrupole ICP-MS analysis of [Np] and [Eu].

2.2.1 Analysis of Quadrupole ICP-MS Data for [Np] and [Eu]

At equilibrium, the partitioning of a chemical species between the aqueous and solid phases of a suspension was described in terms of the distribution coefficient, K_d (e.g. Goto et al., 2008; Kwong-Moses, 2017). In the present study, the K_d value was defined as the ratio of the radionuclide's concentration (Np or Eu) in the solid phase to the concentration of that radionuclide in the aqueous phase, in units of kg/L:

$$K_d = \frac{[R]_{solid\ phase}}{[R]_{aqueous\ phase}},$$

Where $[R]$ was the concentration of the radionuclide of interest. Because the aliquots in this experiment used for quadrupole ICP-MS analysis were diluted with HNO_3 prior to analysis, a dilution correction was necessary for the quantities “ $[R]_{aqueous\ phase}$ ”, and “ $[R]_{solid\ phase}$ ” for the above equation to be used effectively:

$$[R]_{aqueous\ phase} = [R]_{ICP-MS} \times \frac{m_\beta}{m_\alpha},$$

Where “ $[R]_{ICP-MS}$ ” was the concentration of radionuclide measured directly by the ICP-MS, “ m_β ” was the mass of the sample measured by the ICP-MS, and “ m_α ” was the mass of the aliquot extracted from the batch sorption test cell for dilution and subsequent ICP-MS analysis.

To correct the “ $[R]_{solid\ phase}$ ” quantity, the concentration of the radionuclide of interest measured in the aqueous phase by the ICP-MS (“ $[R]_{aqueous, t}$ ”) was subtracted from the original concentration of that radionuclide added to the aqueous phase at the beginning of the sorption experiment (“ $[R]_{aqueous, t=0}$ ”). The difference was then multiplied by the ratio of the mass of the sample aliquot (“ m_s ”) to the mass of the CMS SWy-2 Na-montmorillonite in the original batch sorption cell (“ m_c ”):

$$[R]_{solid\ phase} = [R]_{aqueous, t=0} - [R]_{aqueous, t} \times \frac{m_s}{m_c}$$

Values for the concentrations of Np and Eu in each solid phase were plotted against those in the aqueous phase. K_d values for the sorption of Np onto clay were calculated via linear regression of each data set. Because a single concentration of Eu was spiked into each sorption cell, a linear regression could not be used to calculate K_d values. Instead, K_d values were calculated for each individual sorption cell. K_d values for each solid phase were reported as averages of the K_d values calculated for each sorption cell containing that solid phase.

2.3 Kinetic Modeling of the Smectite → Illite Transformation

In addition to the wet chemistry hydrothermal alteration experiments, the kinetics of the smectite → illite transformation were modeled using methods developed by Huang et. al (1993) and described by Elliott and Matisoff (1996). In Huang et. al's model, the loss of smectite (or gain in illite) was approximated by:

$$\frac{\delta S}{\delta t} = -\kappa S^\alpha [K^+]^\beta$$

Where S was the quantity of smectite lost, α was the dimensionless smectite order parameter, β was the dimensionless potassium order parameter, and κ was the Arrhenius-type illitization reaction rate constant in time^{-1} . The Arrhenius-type illitization reaction rate constant was described by:

$$\kappa = A \exp\left(-\frac{E_a}{RT}\right)$$

Where E_a was the activation energy in 28 kcal per mole, A was the pre-exponential constant in time^{-1} (80800 sec^{-1}), R was the gas constant (8.314 Joules/mol K, 0.001987 kcal/(mole K)), and T was the absolute temperature in Kelvin.

For the purpose of this study, Huang et. al's model was applied over a five-month period, with one day as the time step between each calculation, at 200°C (473 K) in a 15 mM K^+ solution. The gain in illite was calculated from the potassium removed from the solution to form illite. The potassium in ppm lost from the solution (gained in the solid phase) to form illite was converted to wt. % K_2O . Finally, the percentage of illite layers was approximated by dividing the wt. % K_2O by the total wt. % K_2O in muscovite (9.13 wt. % K_2O).

2.4 Speciation Modeling of Np(V), Am(III), and Eu(III) in Hydrothermal Alteration

Experiments and Batch Sorption Solutions

The effects of chloride and hydroxide concentrations on the speciation of Np, Am and Eu, a solution with the following conditions was simulated using PHREEQC modeling software (“pH Redox Equilibrium” in C language), developed by the United States Geological Survey (USGS):

Table 2.5 Solution Parameters for Speciation Modeling of Np, Am and Eu via PHREEQC

<i>Table 2.5: Solution Parameters for Speciation Modeling of Np, Am and Eu via PHREEQC</i>	
Parameter	Value
Temperature	25 °C
pH	13
Pe	5
Redox	Based on pe
Units	mol/kgw
Density	1 kg/L
Cl	0.1 M
Na	0.1 M
Np	1.0×10^{-6} M
Am(III)	1.0×10^{-6} M
Eu(III)	1.0×10^{-6} M
Density of Water	1 kg/L

Within the solution outlined in *Table 2.5*, a reaction was simulated wherein ~0.13 moles of HCl were added iteratively over the course of 2,000 steps, causing the solution to drop from pH 13 to ~pH 6.5. The concentrations of Np, Am, and Eu complexes that formed during the simulated reaction were plotted as a function of solution pH.

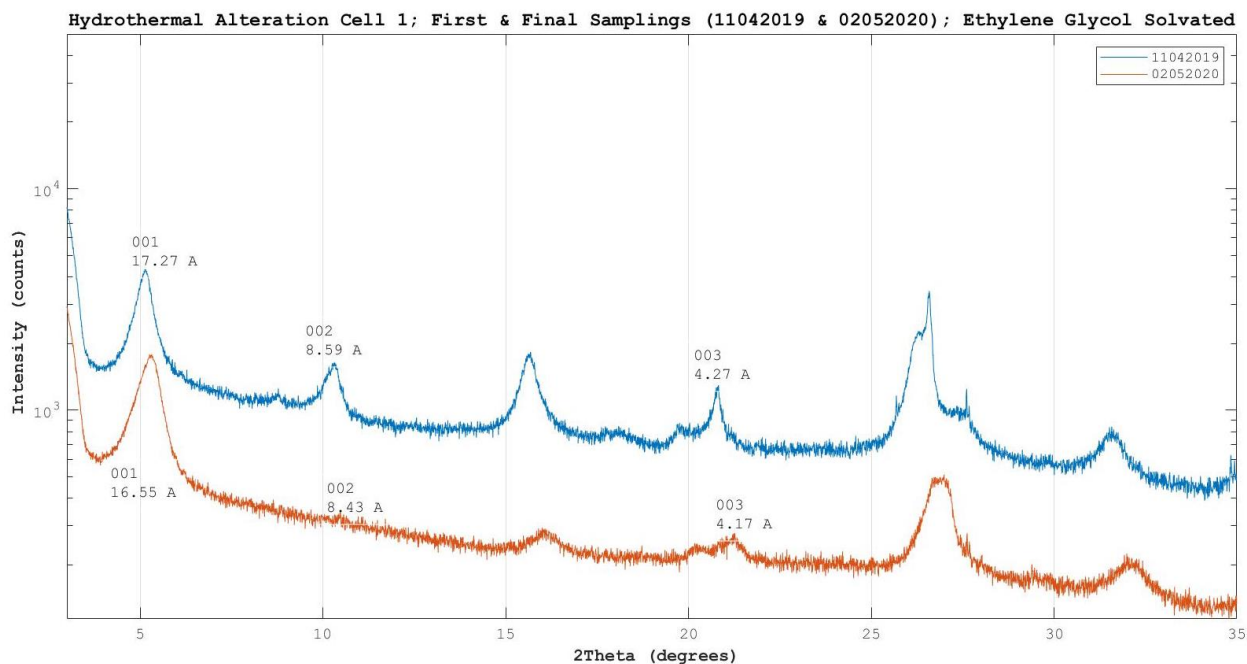
3 RESULTS

3.1 Hydrothermal Alteration Experiment

3.1.1 Extent of Interstratification in SWy-2 Na-montmorillonite

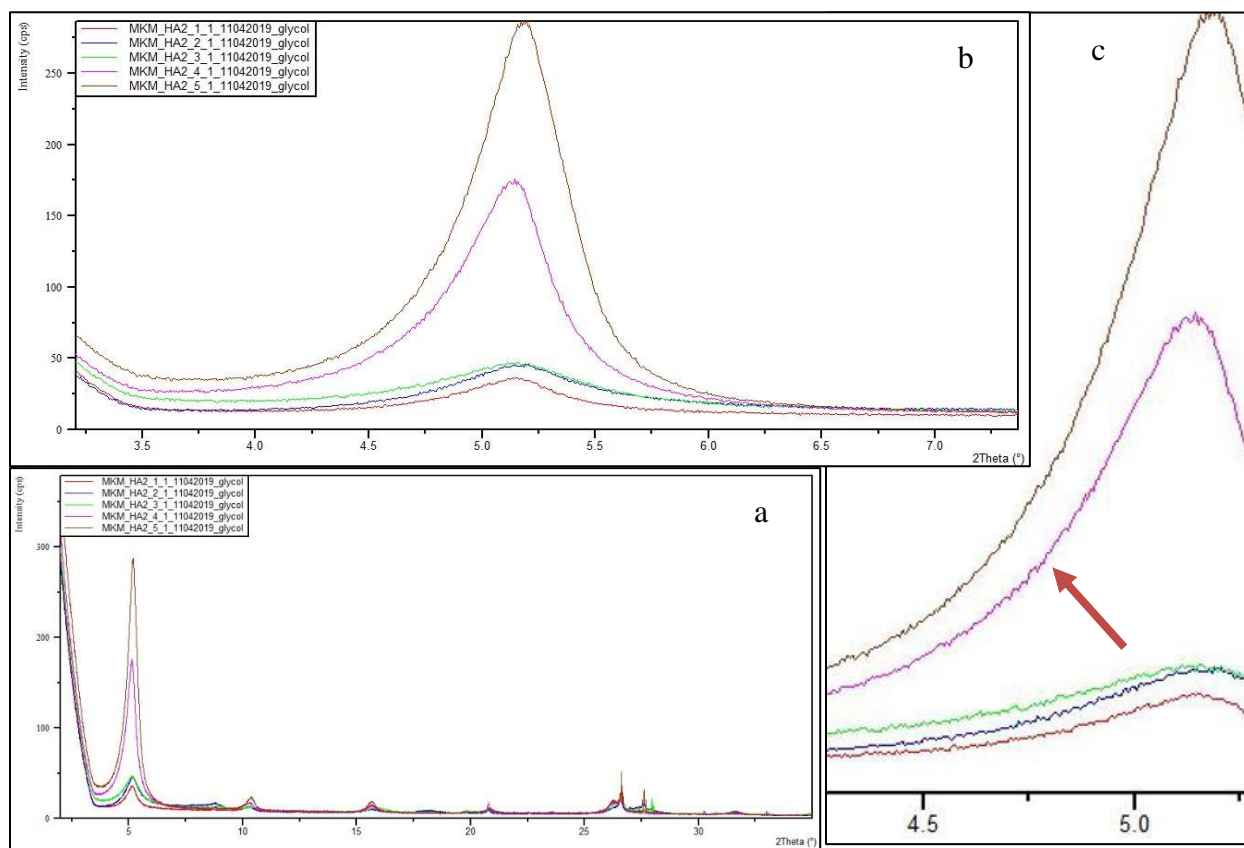
The X-ray diffraction (XRD) patterns for ethylene glycol-solvated samples were used to measure the extent of interstratification created in these hydrothermal alteration experiments. XRD patterns collected throughout the experiment closely resembled one another (*Appendix A.1*). The positions of the 17Å peak and its other 00*l* reflections remained relatively constant for the duration of the experiment, with no definite migration of any particular reflection (*Figure 3.1*, below). The X-ray diffraction data overall showed very little, if any, formation of diagenetic illite in these hydrothermal experiments on the SWy-2 materials having variable K⁺ contents (*Table 3.1*).

Figure 3.1 Overlay of Diffraction Patterns for Ethylene Glycol-Solvated Samples (Reaction cell MKM-HA2-1, after 1 and 14 weeks of hydrothermal alteration).



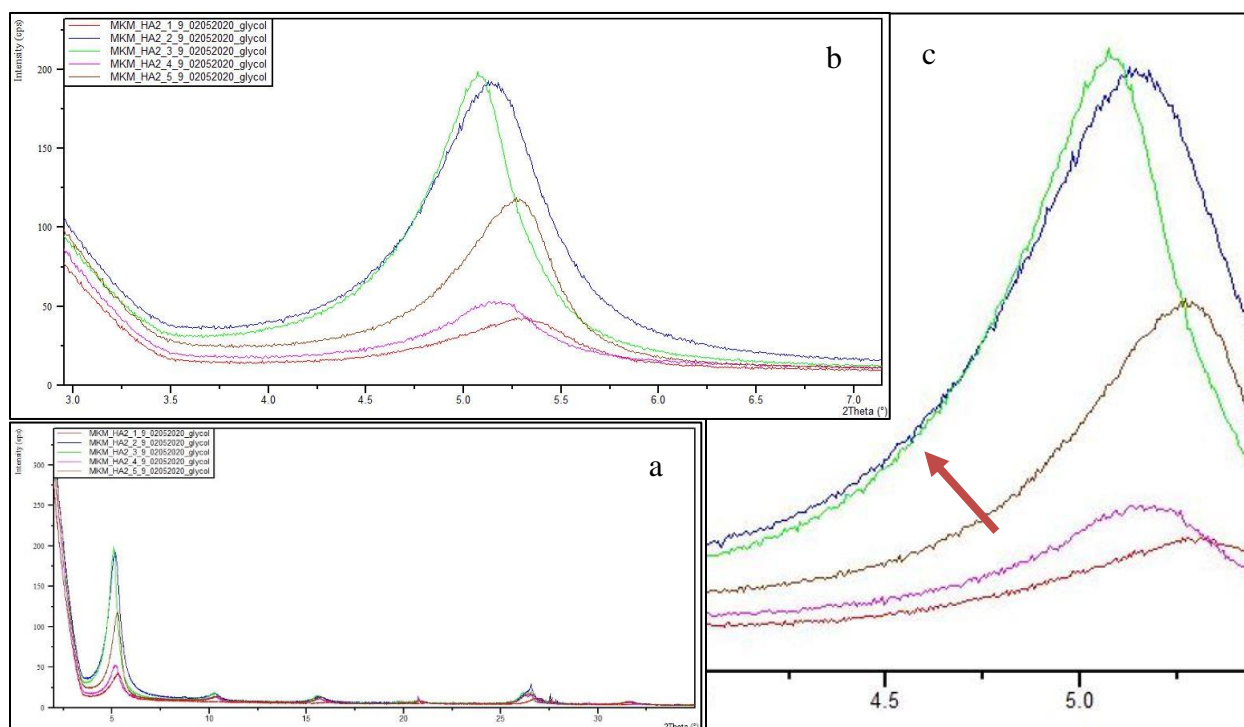
The saddle/peak intensity ratios of the 17Å peak appeared to gradually increase over reaction time, with the saddle intensity slowly rising with respect to the intensity of the 17Å peak. However, plotting experimental 17Å saddle/peak intensity ratios against John Hower's unpublished plot (*Figure 2.7*) yielded neither a discernable trend in the increase in the percentage of illite in the SWy-2 materials, nor in the definite values for percentage of illite layers. Oscillations in signal intensity (peak “chatter”) for the measured peaks became more apparent as the experiment progressed, and asymmetry of the 17Å peak grew more pronounced with time (*Figures 3.2 and 3.3*; red arrows).

Figure 3.2 Magnified 17Å Peak of Ethylene Glycol-Solvated CMS SWy-2 Na-montmorillonite (Reaction Cells MKM-HA2-1-1 – MKM-HA2-1-5) after 1 Week of Hydrothermal Alteration



The entire diffraction pattern generated by the PANalytical software (“a”), the magnified 17Å peak (“b”), and further magnification of the 17Å peak on the high d-spacing side (“c”) are included in *Figure 3.3* (above). X-ray diffraction of ethylene glycol solvated samples of the unaltered SWy-2 Na-montmorillonite yielded a relatively symmetrical 17Å peak with relatively even intensities (minimal peak “chatter”) (*Figure 3.3*).

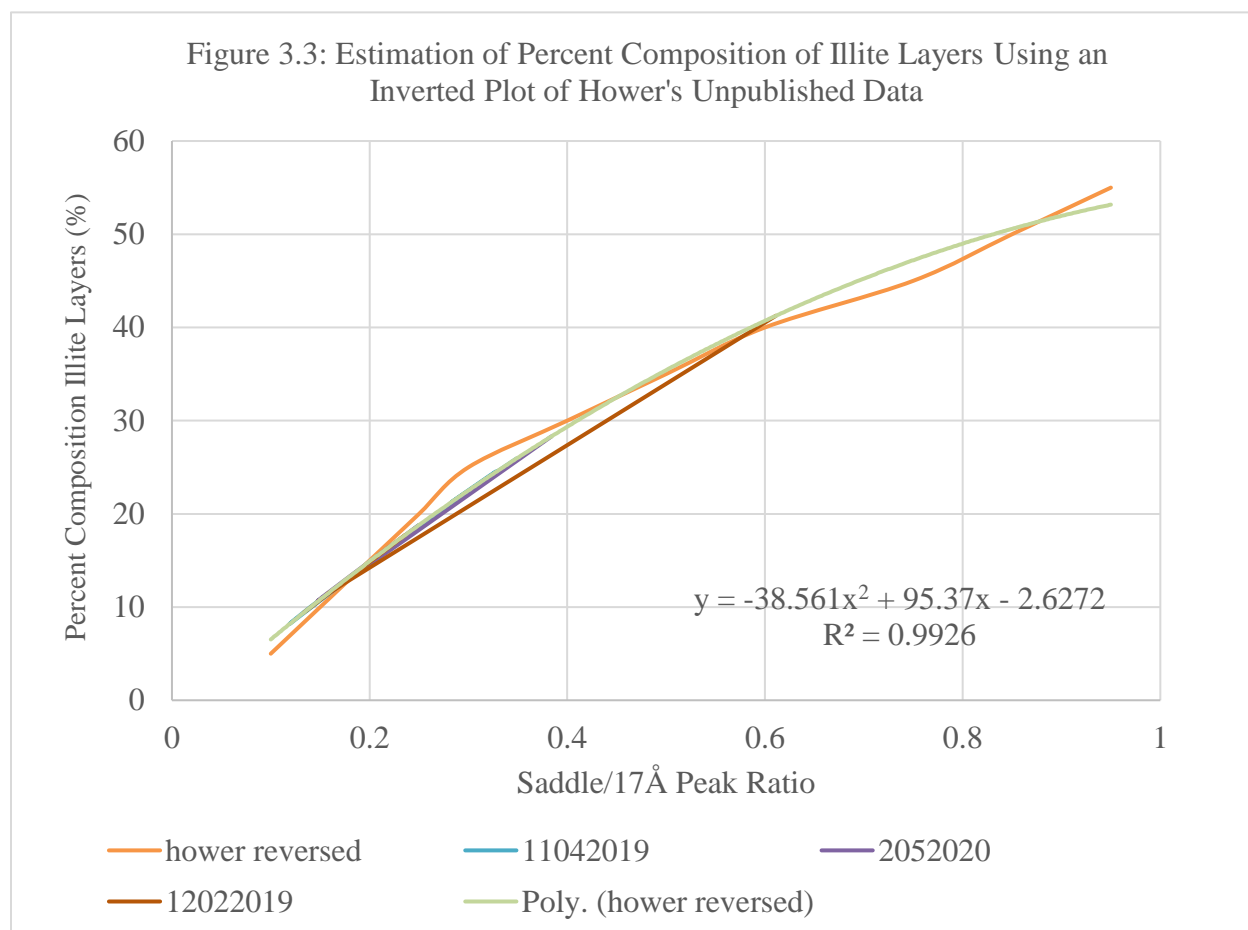
Figure 3.3 Magnified 17Å Peak of Ethylene Glycol-Solvated CMS SWy-2 Na-montmorillonite (Reaction Cells MKM-HA2-1-1 – MKM-HA2-1-5) after 14 Weeks of Hydrothermal Alteration.



The entire diffraction pattern generated by the PANalytical software (Figure 3.2a above), the magnified 17Å peak (Figure 3.2b), and further magnification of the 17Å peak on the high d-spacing side (Figure 3.2c) are included in *Figure 3.2* (above). In semi-quantitative analysis of diffraction patterns obtained for samplings of the hydrothermal alteration experiment, the primary

metric considered was the 17Å peak/saddle intensity ratio, as described by John Hower. In interstratified I/S samples, the 17Å saddle/peak intensity ratio is inversely correlated to the samples' percentage of illite layers.

Figure 3.4 Estimation of Percent Composition of Illite Layers Using an Inverted Plot of Hower's Unpublished Data



Hower's curve was inverted from its original form (*Figure 2.7*) to reflect the percent composition of illite layers as a function of the 17Å saddle/peak intensity ratios (*Figure 3.3*) via extrapolation of points in the original figure. A second-order polynomial was generated to fit the extrapolated points and describe the curve. The 17Å saddle/peak intensity ratios calculated for the

first, midpoint, and final samplings of the present study's hydrothermal alteration experiments were also added to the inverted plot (*Figure 3.3*). All experimental 17\AA saddle/peak intensity ratios (first, midpoint, and final samplings), with the exception of the midpoint sampling of cell 1, corresponded to percent composition illite layers below 30%, with no discernable trend in the data. The percent composition of illite layers for the final sampling that were calculated in this manner did not appear to be greater than those calculated for the first sampling. However, the lack of consistency or trends between calculated values for percent composition of illite layers in the hydrothermal alteration cells over the course of the experiment suggests that no illitization occurred.

3.1.2 Differential 2Θ ($^{\circ}2\Theta$) Values for 001/002 and 002/003 Reflections

Differential 2Θ values that were calculated for the hydrothermal alteration cells at samplings 1 (November 4, 2019), 5 (December 12, 2019), and 9 (February 5, 2020) largely corresponded to less than 10% composition of illite layers (*Table 3.1*). No trend was apparent in this data, which suggested minimal, if any, illitization.

Table 3.1 Calculated Differential 2Θ ($^{\circ}\Delta\Theta$) Values for Experimental 001/002 with 002/003 Reflections & 17\AA Saddle/Peak Intensity Ratios with Corresponding Percent Composition of Illite Layers.

Table 3.1: Calculated Differential 2Θ ($^{\circ}\Delta\Theta$) Values with Percent Composition of Illite Layers for Experimental 001/002 and 002/003 Reflections & 17\AA Saddle/Peak Intensity Ratios with Corresponding Percent Composition of Illite Layers											
Sampling	Sample	001 Position ($^{\circ}2\Theta$)	001/002	%I (001/002)	002/003	%I (002/003)	$^{\circ}\Delta 2\Theta$	%I ($^{\circ}\Delta 2\Theta$)	17\AA Saddle/Peak Intensity Ratio	%I (17\AA Saddle/Peak Intensity Ratio)	
1: 11042019	1-1	5.152	10.34	<10%	15.68	<10%	5.34	<10%	0.3486	25.93	
	2-1	5.191	10.25	16.27	15.61	<10%	5.36	<10%	0.2827	21.25	
	3-1	5.132	10.39	<10%	15.90	20.89	5.51	13.13	0.3243	24.25	
	4-1	5.158	10.29	13.11	15.65	<10%	5.36	<10%	0.1521	10.99	
	5-1	5.132	10.37	<10%	15.64	<10%	5.27	<10%	0.1203	8.287	
5: 12022019	1-5	5.020	10.02	33.41	15.41	<10%	5.39	<10%	0.6111	41.25	
	2-5	5.092	10.23	17.83	15.62	<10%	5.39	<10%	0.1570	11.39	
	3-5	5.092	10.27	14.69	15.68	<10%	5.41	<10%	0.2359	17.72	
	4-5	*									
	5-5	5.086	10.32	10.70	15.58	<10%	5.26	<10%	0.1332	9.389	
9: 02052020	1-9	5.355	10.52	<10%	16.00	28.07	5.48	11.93	0.2493	18.75	
	2-9	5.099	10.25	16.27	15.64	<10%	5.39	<10%	0.1902	14.12	
	3-9	5.132	10.25	16.27	15.56	<10%	5.31	<10%	0.1521	10.99	
	4-9	5.198	10.30	12.31	15.65	<10%	5.35	<10%	0.3842	28.32	
	5-9	5.27	10.39	<10%	15.76	10.22	5.37	<10%	0.2493	18.75	

*Diffraction pattern for sample 4-5 was unable to be recovered (COVID-19)

3.2 Batch Sorption Experiments

3.2.1 Sorption of Neptunium onto Hydrothermal Alteration Products and Unaltered SWy-2 Na-montmorillonite

The partitioning coefficient, K_d , described the sorption radionuclides onto the clay, in units of kg/L. In the case of Np, K_d values spanned a wide range of orders of magnitude from 10^2 to 10^6

(Table 3.2). No trend in the data was recognized. Additionally, the K_d values for the sorption of Np onto the clay samples were calculated using a linear regression of data from additions of a range of Np concentrations. Because only one batch sorption cell could be constructed using solid phase two, there was sorption data for only a single concentration of Np. Consequently, a linear regression could not be applied to this single data point, and a K_d value could not be calculated for this solid phase. Isotherms for the neptunium batch sorption experiments were included in Appendix B.1.

Table 3.2 K_d Values for Sorption of Np onto Hydrothermal Alteration Products and Unaltered SWy-2 Na-montmorillonite

Table 3.2: K_d Values for Sorption of Np onto Hydrothermal Alteration Products and Unaltered SWy-2 Na-montmorillonite			
<i>Solid Phase</i>	<i>Alteration Conditions</i>	<i>K_d (L/kg)</i>	<i>Uncertainty</i>
<i>1 (MKM-HA2-1)</i>	15 mM KOH at 200°C	1.50×10^6	1.98×10^4
<i>2 (MKM-HA2-2)</i>	15 mM KOH at 200°C	*	*
<i>3 (MKM-HA2-3)</i>	15 mM KCl at 200°C	1.54×10^6	5.18×10^3
<i>4 (MKM-HA2-4)</i>	15 mM KCl at 200°C	3.05×10^2	7.06×10^2
<i>5 (MKM-HA2-5)</i>	DI H ₂ O at 200°C	4.57×10^4	1.76×10^4
<i>6 (Unaltered SWy-2 Na-montmorillonite)</i>	N/A	1.04×10^3	4.23×10^2
<i>*K_d value could not be calculated using a linear regression of data from a single batch sorption cell.</i>			

3.2.2 Sorption of Europium onto Hydrothermal Alteration Products and Unaltered SWy-2 Na-montmorillonite

The partition coefficient values, K_d , that were calculated for the sorption of Eu onto each solid phase were on the order of 10^5 - 10^6 for the first sampling of the batch sorption cells and decreased to the order of magnitude of 10^3 - 10^4 by the second sampling (*Table 3.3*).

The K_d values for the sorption of Eu onto the solid phases were calculated as average. It was, not possible to calculate standard deviations for the K_d value associated with solid phase 2, because, again, there was only a single sorption cell constructed with solid phase 2, and thus, only a single K_d value was calculated. Isotherms for the europium batch sorption experiments were included in *Appendix B.2*.

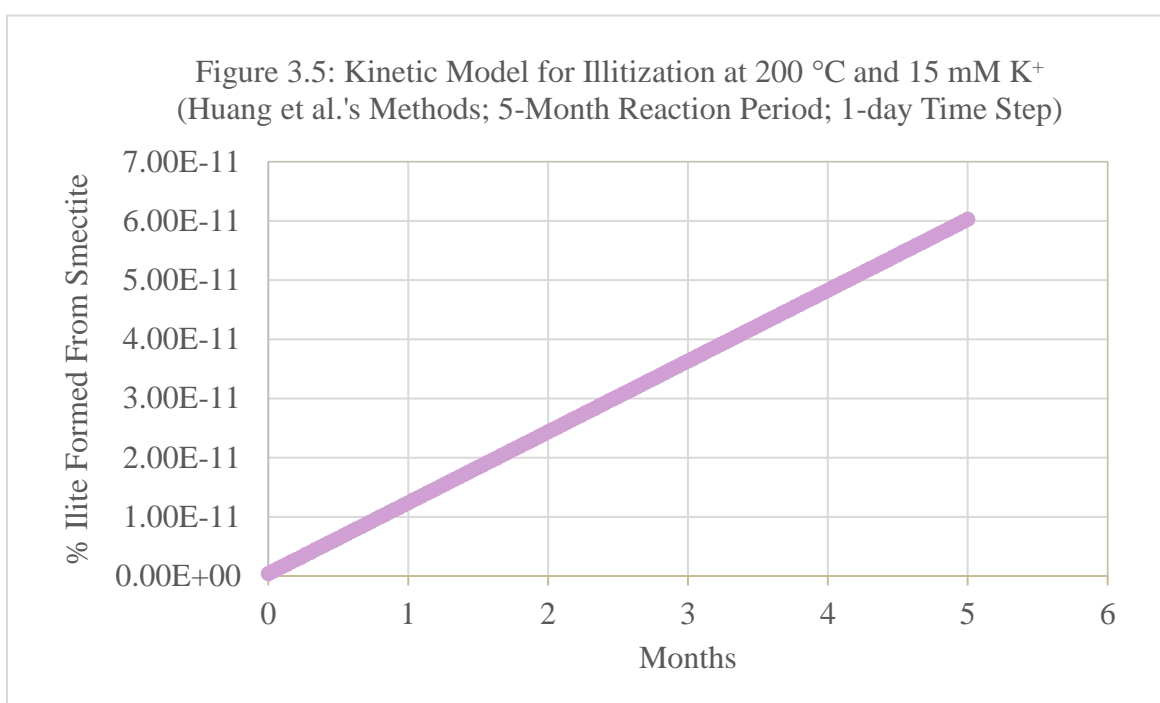
Table 3.3 K_d Values for Sorption of Eu onto Hydrothermal Alteration Products and Unaltered SWy-2 Na-montmorillonite

Table 3.3: K_d Values for Sorption of Eu onto Hydrothermal Alteration Products and Unaltered SWy-2 Na-montmorillonite					
<i>Solid Phase</i>	<i>Alteration Conditions</i>	K_d (L/kg, S1)	Standard Deviation (S1)	K_d (L/kg, S2)	Standard Deviation (S2)
1 (MKM-HA2-1)	15 mM KOH, 200°C	1.40×10^5	2.54×10^4	1.80×10^4	5.17×10^3
2 (MKM-HA2-2)	15 mM KOH, 200°C	1.69×10^5	*	1.08×10^4	*
3 (MKM-HA2-3)	15 mM KCl, 200°C	1.94×10^5	4.43×10^4	2.48×10^4	4.13×10^3
4 (MKM-HA2-4)	15 mM KCl, 200°C	2.37×10^5	2.89×10^4	2.43×10^4	5.95×10^3
5 (MKM-HA2-5)	DI H ₂ O, 200°C	2.07×10^5	4.53×10^4	1.79×10^3	1.97×10^2
6 (Unaltered SWy-2 Na-montmorillonite)	N/A	1.30×10^6	1.11×10^6	3.55×10^4	2.47×10^4
<i>*Standard deviations could not be calculated for the single K_d value derived from one batch sorption cell.</i>					

3.3 Kinetic Modeling of the Smectite → Illite Transformation

The model results shown below (*Figure 3.5*) showed very little illite formed under these conditions. These results were consistent with X-ray diffractometry, the results of which also did not show any formation of diagenetic illite.

Figure 3.5 Kinetic Model for Illitization at 200 °C and 15 mM K⁺ (Huang et al.'s Methods; 5-Month Reaction Period; 1-day Time Step)



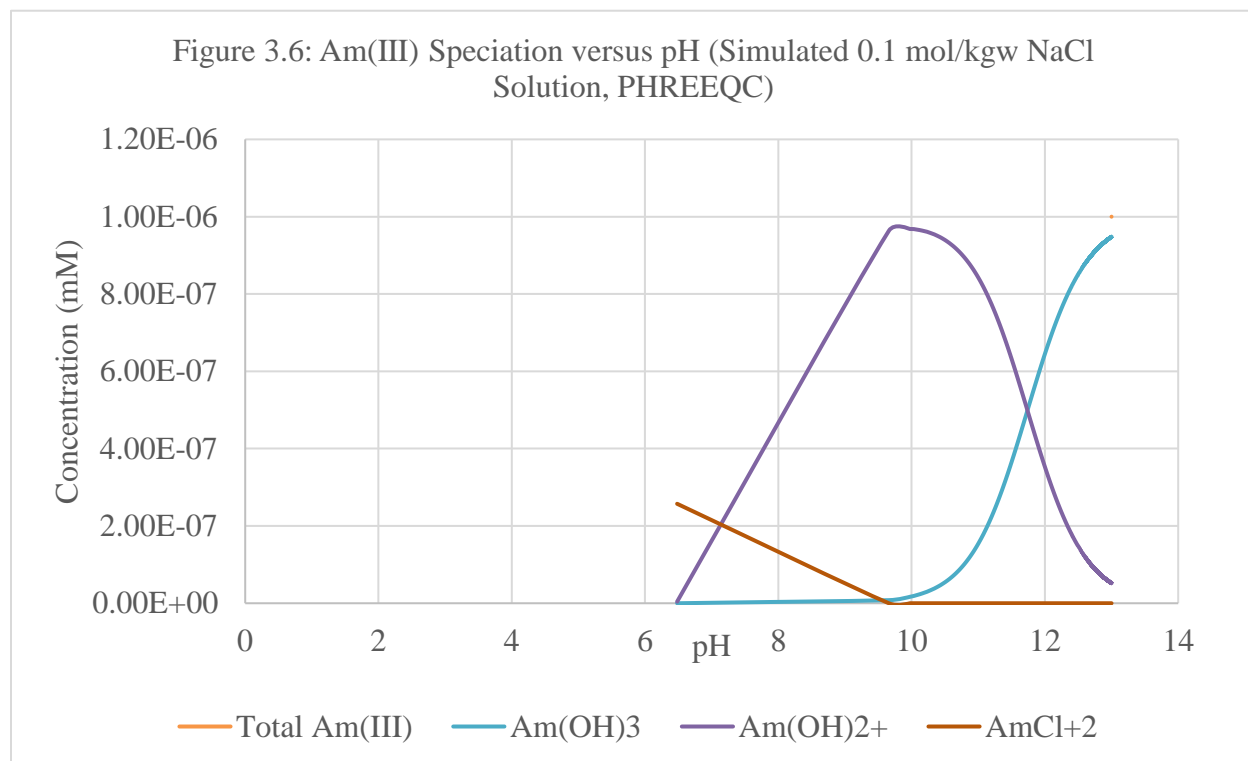
For the purposes of this study, the first three months of the kinetic model's results were relevant. Although Huang et al.'s methods describe illitization as a second-order reaction, the very small (undetectable by conventional means) percentages of illite formed over this short period appear to assume a linear trend. Additionally, the percent illite formed from smectite over this time period was extremely minimal, if not negligible. Modeling results for 200 ppm K⁺ at 125 °C over a period of 100,000 years indicated that 30% illite can be formed from smectite.

3.4 Speciation Modeling of Am(III), Eu(III) and Np(V) in Batch Sorption Solutions

The Am(III), Eu(III) and Np(V) complexes that formed in the model solution were $\text{Am}(\text{OH})_3$, $\text{Am}(\text{OH})^{2+}$, $\text{Am}(\text{Cl})^{2+}$, EuO_2^- , EuO_2H^- , EuO^+ , $\text{Eu}(\text{OH})^{2+}$, EuCl_2^{2+} , EuCl_2^+ , $\text{Eu}_2(\text{OH})_2^{4+}$, EuCl_3 , EuCl_4^- , NpO_2^+ , NpO_2OH , and $\text{NpO}_2(\text{OH})^{2-}$ (Figures 3.6, 3.7 and 3.8).

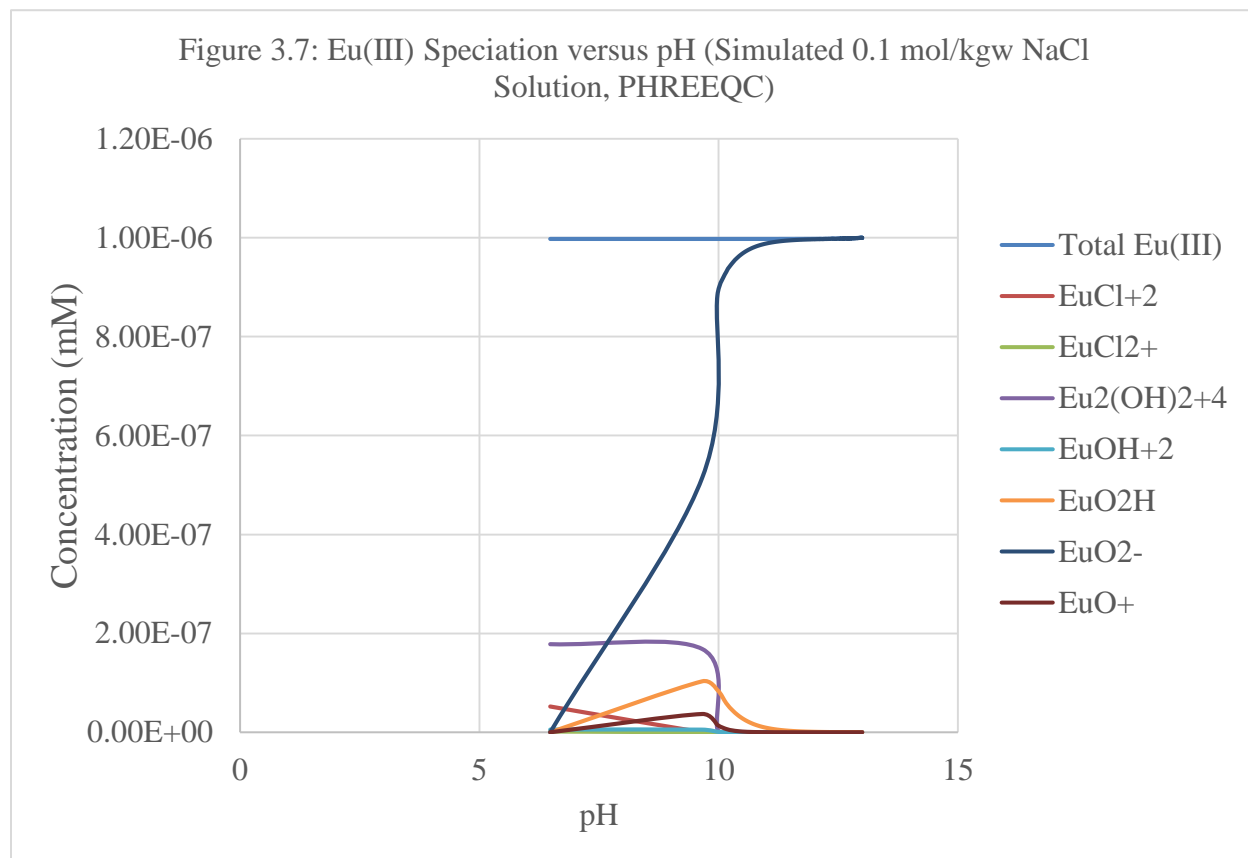
At $\text{pH} > \sim 11.5$, Am(III) complexes in the simulated solution were comprised of $\text{Am}(\text{OH})_3$, $\text{Am}(\text{OH})^{2+}$, and $\text{Am}(\text{Cl})^{2+}$ (Figure 3.6, below). The concentration of $\text{Am}(\text{OH})_3$ decreased as the pH was lowered by the addition of HCl, $\text{Am}(\text{OH})^{2+}$ concentration increased with decreasing pH, and the concentration of $\text{Am}(\text{Cl})^{2+}$ was minimal and increased slightly. At $\sim \text{pH} 11.5$, there was a convergence of the concentrations of $\text{Am}(\text{OH})_3$ and $\text{Am}(\text{OH})^{2+}$ concentrations and $\text{Am}(\text{Cl})^{2+}$. At $\sim \text{pH} 10$, the concentration $\text{Am}(\text{OH})_3$ approached zero, and the concentration of $\text{Am}(\text{OH})^{2+}$ reached a maximum and began to rapidly decrease, eventually reaching zero at $\sim \text{pH} 6.5$.

Figure 3.6 Am(III) Speciation versus pH (Simulated 0.1 mol/kgw NaCl Solution, PHREEQC)



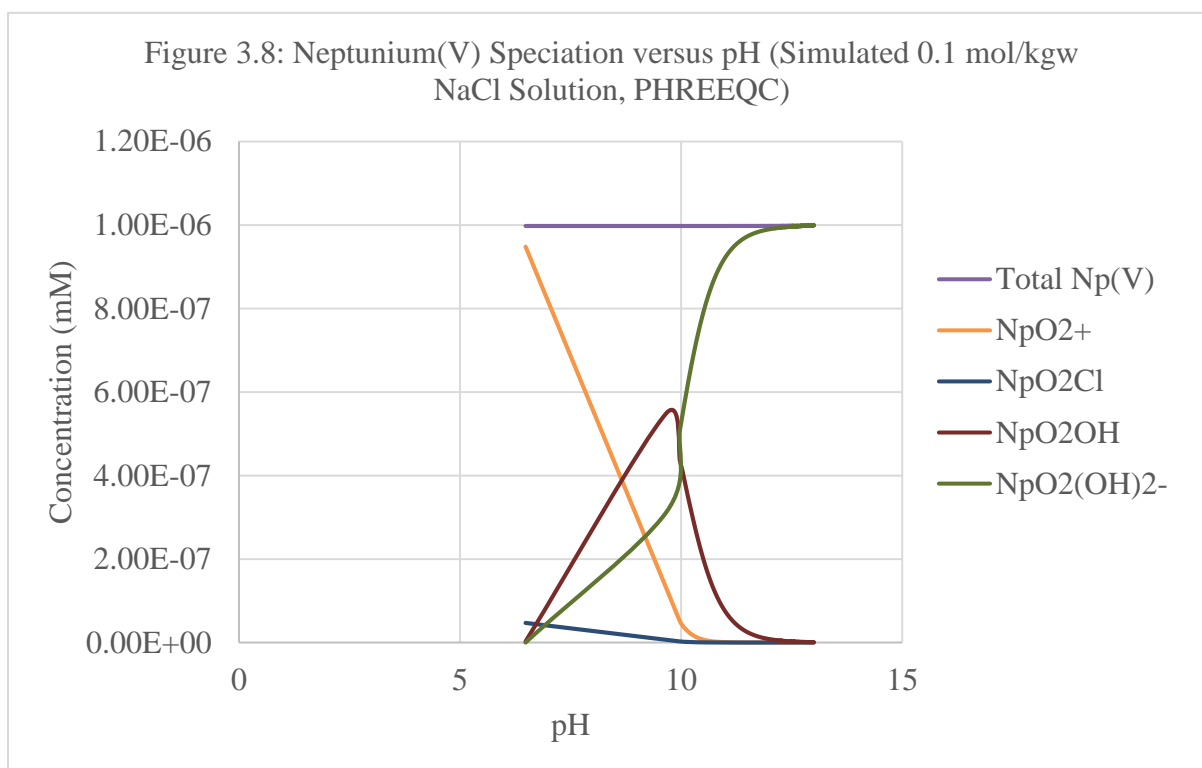
Europium(III) complexes in the simulated solution were comprised of EuO^{2-} , EuO_2H , EuO^+ , EuOH^{2+} , EuCl_2^+ , EuCl_2^{2+} , $\text{Eu}_2(\text{OH})_2^{4+}$, EuCl_3 , EuCl_4^- (Figure 3.7, below). EuO_2H , EuO^+ , and EuCl_2^+ concentrations were minimal, but increased with decreasing pH, spiking at pH 9.5. The concentration of EuO^{2-} decreased as the solution became more acidic. From pH 13 to pH ~ 10, the concentration of EuO^{2-} decreased exponentially, after which it decreased at a roughly linear rate with an inflection point at pH ~ 9.

Figure 3.7 Eu(III) Speciation versus pH (Simulated 0.1 mol/kgw NaCl Solution, PHREEQC)



In this study, Np(V) complexes were of interest. These complexes in solution were NpO_2^+ , NpO_2OH , and $\text{NpO}_2(\text{OH})_2^-$ (Figure 3.8, below). Data for $\text{NpO}_2(\text{OH})_2^-$ was shown in red. The concentration of $\text{NpO}_2(\text{OH})_2^-$ decreased as the solution became more acidic. Concentrations of NpO_2^+ and NpO_2OH increased with solution acidity.

Figure 3.8 Neptunium(V) Speciation versus pH (Simulated 0.1 mol/kgw NaCl Solution, PHREEQC)



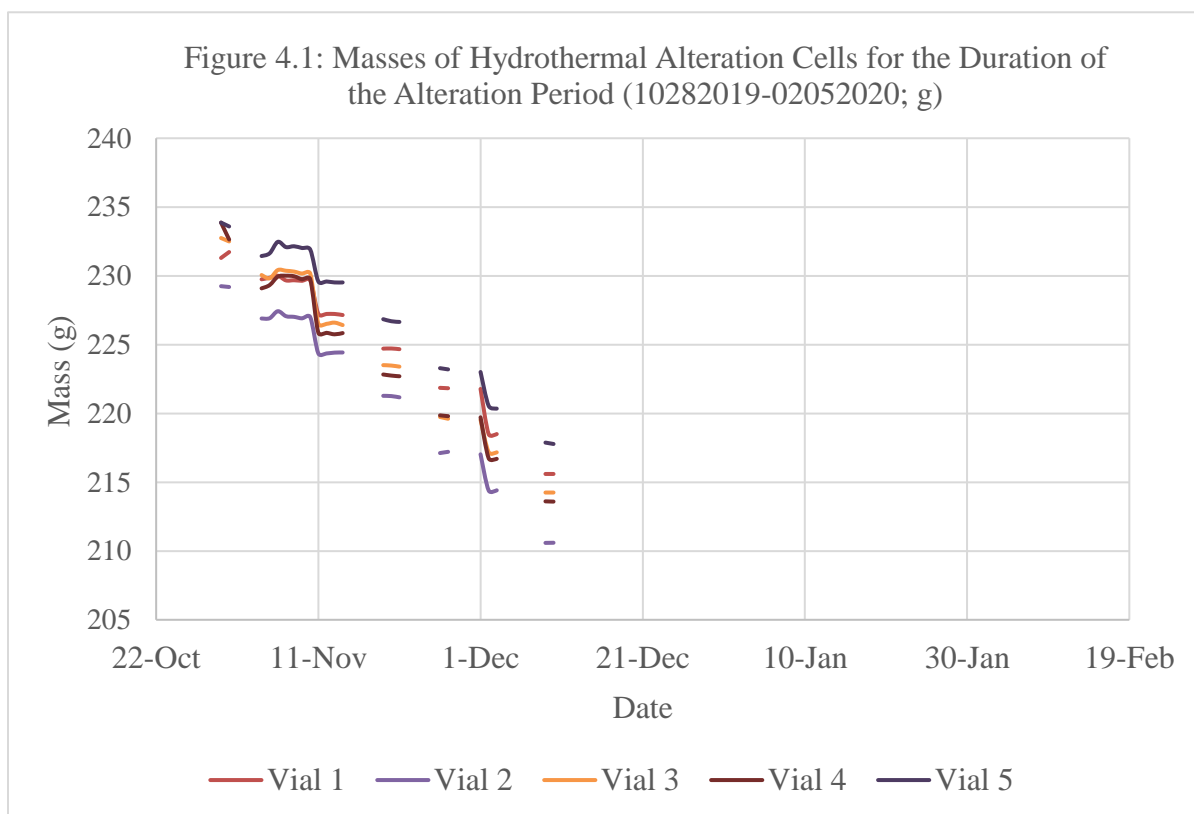
4 DISCUSSION

4.1 Hydrothermal Alteration Experiments

4.1.1 Possible Solution Loss from Hydrothermal Alteration Cells via Evaporation

Because the PTFE vials used for the hydrothermal alteration experiments did not prove to be vapor-tight over the course of preliminary experiments, the masses of each alteration cell (solid phase, plus aqueous phase, plus vial and lid) were recorded periodically to track possible solution loss via evaporation (*Figure 4.1*).

Figure 4.1 Masses of Hydrothermal Alteration Cells for the Duration of the Alteration Period (10282019-02052020).



The masses of the cells were relatively stable over the course of the reaction; however, for samplings of reaction cells, approximately 2.0 g of the cell contents (mix of solid and aqueous

phases) were removed at a time. The vials were rehydrated once with 5 mL DI H₂O after the 7th sampling event (January 24, 2020). In general, it was assumed that the solid: solution ratios of the alteration cells did not change appreciably over the course of the reaction period.

4.1.2 Inconsistencies in X-ray Diffraction Patterns

4.1.2.1 Variations in Peak Intensity

Examination of the diffraction patterns obtained from samples of the hydrothermal alteration cells revealed inconsistencies in the intensities of peaks. These inconsistencies correlated to the amount of material that was used to construct each slide for diffraction analysis. Because semi-quantitative analyses of X-ray diffraction patterns utilized intensity ratios rather than intensity magnitudes, it was assumed that the varied intensities of peaks did not impact the veracity of any conclusions drawn.

4.1.2.2 Variations in Peak Positions and Assessment of Possible Goniometer Misalignment

In addition to varied intensities of peaks, the diffraction patterns from the hydrothermal alteration cells also displayed inconsistencies in peak positions. Such inconsistencies may have been the result of goniometer alignment issues. The 4.26Å and 3.34Å peaks for the measured quartz standard (“Quartz Standard_02102020”, *Figure 2.2*) were shifted 0.04° and 0.09° 2 θ towards the high °2 θ side of the diffraction pattern, compared to the reference standard “Spruce Claim Quartz Standard (RRUFF)”, (*Figures 2.2 and 2.3, Table 2.2*). These observed shifts suggested a minor degree of goniometer misalignment, or vertical displacement for the diffraction patterns in the present study, which may have, in turn, affected positions of peaks included on diffraction patterns obtained for hydrothermal alteration products. Because the quartz standard was only measured once, rather than several times over the course of the diffraction data collecting

period, corrections to d-spacing values measured for the hydrothermal alteration samplings were omitted from this study.

4.1.3 Semi-Quantitative Results from X-ray Diffraction

4.1.3.1 17Å Saddle/Peak Intensity Ratio

The 17Å saddle/peak intensity ratio (devised by John Hower) was used to estimate the percentage composition of illite layers in an interstratified smectite/illite sample.

The 17Å saddle/peak intensity ratios for this study's hydrothermal alteration starting material and end products were superimposed onto a version of Hower's plot with its axes reversed (Figure 3.5). Neither patterns nor trends in the experimental the 17Å saddle/peak intensity ratios were apparent—end products did not appear to have higher saddle/peak intensity ratios than the starting material. Instead, the saddle/peak intensity ratios for both the starting material and the end products clustered around 0-0.4. This range corresponded to 0-30% composition of illite layers. This clustering and the lack of a trend in the experimental 17Å saddle/peak intensity ratio data suggested that no illite layers were formed during this study's hydrothermal alteration experiment.

4.1.3.2 Differential 2Θ (°Δ2Θ) Values for 001/002 and 002/003 Reflections

The percent composition of illite layers present in an I/S bearing sample can be estimated accurately via calculation and analysis of differential 2Θ values (Moore and Reynolds, 1997). However, implementation of Moore and Reynolds' methods requires very accurate and precise diffraction data. Moore and Reynolds' methods were applied to the diffraction data for samplings 1, 5 and 9 for the sake of completeness (*Table 3.1*). Estimations of % I calculated in this matter were almost exclusively negative values (reported as <10% illite) which is indicative of both inaccurate/imprecise diffraction data, and the lack of illite formation.

4.1.4 Qualitative Results from X-ray Diffraction

4.1.4.1 17Å Peak Intensity Oscillations

The severity of oscillations in signal intensity (counts per second) on the 17Å peak of an ethylene-glycol solvated smectite sample was used as an indicator of interstratification, or at a minimum, changes within the smectite structure. Close examination of the diffraction patterns for the hydrothermal alteration end products (ninth sampling; February 5, 2020) and comparison against those from the first sampling (November 4, 2019) revealed an increase in the severity of signal intensity oscillations. This increase in severity was indicative of minor amounts of change to the smectite structure as a result of the alteration.

4.2 Batch Sorption Experiments

4.2.1 Sorption of Neptunium onto Hydrothermal Alteration Products and Unaltered SWy-2 Na-montmorillonite

K_d values calculated for the sorption of Np onto each solid phase did not appear to be dependent on the alteration conditions to which each solid phase was subjected (*Table 3.2*). Solid phases 1 and 3 yielded the highest K_d values; however, solid phases 1 and 3 were treated with 15 mM KOH and 15 mM KCl, respectively. Solid phase 4, which was replicate of solid phases 3 in terms of alteration conditions, yielded a K_d value four orders of magnitude less than solid phase 3. This suggested that the neptunium was sorbed more preferentially to solid phase 3 versus solid phase 4, despite both solid phases' exposure to the same alteration conditions.

Likewise, it should be noted that solid phase 2 was a replicate of solid phase 1 in terms of alteration conditions. However, K_d values for the sorption of Np onto solid phase 2 could not be calculated via linear regression because the batch sorption experiment only included one cell and thus a single concentration of Np for solid phase 2.

4.2.2 Sorption of Europium onto Hydrothermal Alteration Products and Unaltered SWy-2 Na-montmorillonite

K_d values calculated for the sorption of Eu onto each solid phase appeared to be independent of each solid phases' alteration conditions (Table 3.3). The K_d values calculated for the second sampling of the batch sorption experiment were approximately one order of magnitude less than those calculated for the first sampling. This suggested desorption of the Eu from each solid phase.

It was not possible to calculate standard deviations for the K_d values associated with solid phase 2, because, again, only a single sorption cell was constructed using solid phase 2.

4.2.3 pH Measurements of Individual Batch Sorption Cells

Measured values for pH of the individual sorption cells remained near 7 and did not vary considerably between cells containing solid phases 1-5. However, cells containing solid phase 6 were buffered to about pH 9. As discussed below, the higher pH values resulted in greater sorption of Eu and Np. K_d values for the sorption of neptunium and europium onto solid phase 6 (unaltered SWy-2 Na-montmorillonite) were higher than those for the sorption of neptunium and europium onto the other solid phases. Thus, hydrothermal alteration, pH values, and by extension, speciation of neptunium and europium may have affected the sorption of stable Eu and ^{237}Np onto the alteration products.

Table 4.1 pH Measurements of Individual Batch Sorption Cells

Table 4.1: pH Measurements of Individual Batch Sorption Cells				
		Date		
Cell Group/Solid Phase	Sample ID	02272020	03052020	05012020
<i>1</i>	1-1	6.62	7.31	7.02
	1-2	7.13	7.23	7.04

	1-3	7.43	7.25	7.03
	1-4	7.39	7.06	6.92
	1-5	7.02	7.11	6.98
2	2-5	7.09	6.91	7.09
3	3-1	7.41	7.16	7.07
	3-2	7.2	7.18	7.08
	3-3	7.47	7.16	7.02
	3-4	7.1	7.13	7.04
	3-5	7.08	7.07	6.98
4	4-1	7	7.04	6.96
	4-2	6.81	6.96	6.93
	4-3	7.02	6.94	6.93
	4-4	6.94	6.88	6.9
	4-5	6.9	6.76	6.81
5	5-1	6.95	6.85	6.86
	5-2	6.68	6.71	6.76
	5-3	7.01	6.72	6.78
	5-4	6.75	6.85	6.92
	5-5	6.74	6.55	6.62
6	6-1	8.28	8.89	8.65
	6-2	8.01	9.05	8.94
	6-3	8.86	8.64	8.55
	6-4	9.09	8.14	8.48
	6-5	8.59	8.95	8.67

4.3 Kinetic Modeling of the Smectite → Illite Transformation and Comparison Against Results of the Hydrothermal Alteration Experiment

Modeling the loss in smectite (or gain in illite) per Huang et al.'s methods over a five-month reaction period yielded extremely minimal, if not negligible, percent composition of illite. This result reinforced the results of the hydrothermal alteration experiments by suggesting that measurable illite formation was not possible over the hydrothermal reaction period under the temperature and solution conditions used.

4.4 Speciation Modeling of Am(III), Eu(III), and Np in Batch Sorption Solutions

The data yielded from the speciation modeling was used to predict the speciation of Am(III), Eu(III) and Np(V) in the batch sorption cells which reacted these elements with the hydrothermal alteration experiments and samples of the unaltered SWy-2 Na-montmorillonite. Measurements of the batch sorption cells' pH were taken upon construction—the cells had pH values ranging from ~6.62 - ~9.09. Thus, the speciation modeling data was considered over this pH range.

In terms of Am(III), the presence of chloride in solution did not appear to substantially affect speciation. However, the presence of the hydroxide ion seemed very important in Am(III) speciation. From pH ~6.5 – pH ~11.5, $\text{Am}(\text{OH})_2^+$ was the dominant species, and from pH ~ 11.5 – pH 13, $\text{Am}(\text{OH})_3$ became more prevalent. Over the pH range seen in the batch sorption cells, the concentration of $\text{Am}(\text{OH})_2^+$ increased at a nearly linear rate, and no other Am(III) complexes were present at significant concentrations.

Eu(III) complexes in the modeled solution over the pH range of the batch sorption cells consisted of EuO_2^- , EuO_2H , and EuO^+ . As was the case for Am(III) speciation, this distribution of species suggested that the presence of hydroxide ions influenced Eu(III) speciation, while presence of chloride ion did not.

With regard to Np in the simulated solution, species that were present over the pH range of interest were NpO_2^+ , NpO_2Cl , and $\text{NpO}_2(\text{OH})_2^-$. This distribution suggested that the presence of both the chloride ion and the hydroxide ion contributed to Np(V) speciation.

Comparison of the pH levels of the batch sorption cells against their K_d values for the sorption of Eu and Np, and subsequent inference of the speciation of Eu and Np in each of the cells did not reveal that the sorption of Eu and Np complexes onto the clay was affected by speciation, and by extension, the presence of chloride and hydroxide ions in solution. However, closer monitoring of

the pH levels in each batch sorption cell over the duration of the reaction period was needed to draw more firm conclusions.

5 CONCLUSIONS

The hydrothermal alteration experiments of this study did not induce any significant and measurable illitization of samples of SWy-2 Na-montmorillonite. However, X-ray diffraction of the alteration products indicated that some small amount of interstratification or incipient illitization did occur within the clay, as evidenced by increases in the intensities of the minima occurring on the high d-spacing side of the 17Å peak. In the hydrothermal alteration experiments, samples of the SWy-2 Na-montmorillonite were exposed to two different sources of K⁺: KOH and KCl. Notably, the solids in KOH were at a significantly higher pH; however, the source of the K⁺ did not influence the degree of interstratification that occurred—all alteration samples exhibited a similar, if not equal, extent of interstratification. The lack of illitization that occurred as a result of the hydrothermal alteration was consistent with the results of a kinetic model that was developed for illitization of smectite under the hydrothermal reaction conditions, wherein the model indicated that no illite should have been expected to form under these time, temperature and solution conditions.

When the altered samples of SWy-2 Na-montmorillonite were placed in solution with stable Eu and ²³⁷Np, they were able to effectively sorb these radionuclides almost as well as the samples of unaltered SWy-2 Na-montmorillonite. Thus, the clay's sorptive abilities may have been impacted, but not eliminated, as a result of the hydrothermal alteration. This finding was most consistent with hypothesis 3 of this study, wherein hydrothermal alteration induced interstratification of the clay (although immeasurable), and alteration products were still able to sorb neptunium and europium.

This study also included predictive modeling of Eu(III) and Np(V) speciation that occurred within the batch sorption cells as a function of pH, to determine if the presence of chloride and/or

hydroxide affected the speciation of these radionuclides, and by extension the radionuclides' propensities to be sorbed by the clay. In this speciation modeling, the presence of hydroxide was found to affect the speciation of Eu(III), and the presence of both hydroxide and chloride affected the speciation of Np(V) over the pH range measured in the batch sorption cells and under hydrothermal alteration conditions. Average K_d values ranged from 1.79×10^2 kg/L – 2.37×10^5 kg/L for the sorption of stable Eu onto altered clay, and from 3.05×10^2 kg/L – 1.54×10^6 kg/L for the sorption of ^{237}Np onto altered clay. Average K_d values for the sorption of stable Eu onto the unaltered clay ranged from 3.55×10^4 kg/L – 1.30×10^6 kg/L. For the sorption of ^{237}Np onto the unaltered clay, the K_d value fitted to the linear data was 1.04×10^3 kg/L. K_d values for the sorption of Eu(III) and Np(V) did not vary across the batch sorption cells constructed with solid phases 1-5; however K_d values for solid phase 6 were higher. This variation seemed to be dependent upon pH, and thus on Eu(III) and Np(V) speciation in solution.

The smectite that was subjected to the hypothesized near-field temperature and solution conditions of a deep geologic repository did not undergo measurable illitization. The combination of the observed interstratification and the expected speciation of Eu(III) and Np(V) may have slightly decreased the clay's ability to sorb stable Eu and ^{237}Np . Results of this study ultimately suggest that further experimentation is needed to explore the effects of hydrothermal alteration on the sorption of radionuclides onto bentonite, specifically over longer reaction periods, different solution conditions, and different time/temperature profiles.

REFERENCES

- 112 th Congress. Department of Defense and Full-Year Continuing Appropriations Act, 2011. Washington, DC: Congressional Record, Vol. 157 (2011). 2011.
- Aja, S. On the Thermodynamic Stability of Illite and IS Minerals. *Clays and Clay Minerals* **2019**, 67 (6), 518–536.
- Altaner, S. Calculation of K Diffusional Rates in Bentonite Beds. *Geochimica et Cosmochimica Acta* **1989**, 53, 923–931.
- Altaner, S. Potassium Metasomatism and Diffusion in Cretaceous K-Bentonites from the Disturbed Belt, Northwestern Montana and in the Middle Devonian Tioga K-Bentonite, Eastern U.S.A. University of Illinois at Urbana-Champaign 1985.
- Altaner, S.; Ylagan, R. Comparison of Structural Models of Mixed-Layer Illite/Smectite and Reaction Mechanisms of Smectite Illitization. *Clays and Clay Minerals* **1997**, 45, 517–533.
- Alvarez, R. The WIPP Problem, and What It Means for Defense Nuclear Waste Disposal. Bulletin of the Atomic Scientists 2014.
- Banik, N.; Marsac, R.; Lutzenkirchen, J.; Marquardt, C.; Dardenne, K.; Rothe, J.; Bender, K.; Geckeis, H. Neptunium Sorption and Redox Speciation at the Illite Surface under Highly Saline Conditions. *Geochimica et Cosmochimica Acta* **2017**, 215, 421–431.
- Beauheim, R.; Roberts, R. Hydrology and Hydraulic Properties of a Bedded Evaporite Formation. Sandia National Laboratories 2000.
- Begg, J.; Zavarin, M.; Tumey, S.; Kersting, A. Plutonium Sorption and Desorption Behavior on Bentonite. *Journal of Environmental Radioactivity* **2015**, 141, 106–114.
- Borojevic Sostaric, S.; Neubauer, F. Principle Rock Types for Radioactive Waste

- Repositories. *Rudarsko-geolosko-naftni zbornik* **2012**, 24, 11–18.
- Boyle, C.; Meguid, S. A. Mechanical performance of integrally bonded copper coatings for the long-term disposal of used nuclear fuel. *Nuclear Engineering and Design*. 2015. 293, 403-412.
- Brady, P.; Arnold, B.; Altman, S.; Vaughn, P. Deep Borehole Disposal of Nuclear Waste: Final Report. Sandia National Laboratories. 2012.
- Cheshire, M.; Caporuscio, F.; Rearick, M.; Jove-Colon, C.; McCarney, M. K. Bentonite Evolution at Elevated Pressures and Temperatures: An Experimental Study for Generic Nuclear Repository Designs. *American Mineralogist* **2014**, 99, 1662–1675.
- Culler, F. L. Status Report on the Disposal of Radioactive Wastes. Oak Ridge, TN: Oak Ridge National Laboratory. 1957.
- D'Appolonia Consulting Engineers. Repository Sealing: Evaluations of Materials Research Objectives and Requirments. U.S. Department of Energy June 1980.
- Eberl, D. and Hower, J. Kinetics of Illite Formation. *Geological Society of America Bulletin*. 87(9): 1326-1330. 1976.
- Eberl, D. D.; Velde, B.; McCormick, T. Synthesis of Illite-Smectite from Smectite at Earth Surface Temperatures and High PH. *Clay Minerals* **1993**, 28, 49–60.
- Eberl, D. Reaction Series for Dioctahedral Smectites. *Clays and Clay Minerals* **1978**, 26 (5), 327–340.
- Eberl, D. The Hydrothermal Transformation of Sodium and Potassium Smectite into Mixed-Layer Clay. *Clays and Clay Minerals* **1977**, 25, 215–227.
- Eberl, D.; Hower, J. Kinetics of Illite Formation. *Geological Society of America Bulletin* **1976**, 87, 1326–1330.

- Eberl, D.; Whitney, G.; Khouri, H. Hydrothermal Reactivity of Smectite. *American Mineralogist* **1978**, *63*, 401–409.
- Elliott, W. C. Bentonite Illitization in Two Contrasting Cases: The Denver Basin and the Southern Appalachian Basin, Case Western Reserve University, Cleveland, OH, 1988.
- Elliott, W. C.; Matisoff, G. Evaluation of Kinetic Models for the Smectite to Illite Transformation. *Clays and Clay Minerals* **1996**, *44* (1), 77–87.
- Fairhurst, C.; Adler, H.; Blomeke, J.; Clark, S.; Ernsberger, F.; Ewing, R.; Garrick, J.; Konikow, L.; Krauskope, K.; Roy, D.; et al. *The Waste Isolation Pilot Plant: A Potential Solution for the Disposal of Transuranic Waste*; National Academy Press: Washington, D.C., 1996.
- Fowler, C. S. Native Americans and Yucca Mountain: A Revised and Updated Summary Report on Research Undertaken between 1987 and 1991. Cultural Resource Consultants, Ltd. 1991.
- Frohlich, D.; Kaplan, U. Sorption of Am(III) on clays and clay minerals: A review. *Journal of Radioanalytical and Nuclear Chemistry* **2018**, *318*, 1785-1795.
- Hobart, D. Americium. Lawrence Livermore National Laboratory 2013.
- Hower, J.; Eslinger, E.; Hower, M.; Perry, E. Mechanism of Burial Metamorphism of Argillaceous Sediment: 1. Mineralogical and Chemical Evidence. *Geological Society of America Bulletin* **1976**, *87*, 725–737.
- Huang, W.; Longo, J.; Pevar, D. An Experimentally Derived Kinetic Model for Smectite-to-Illite Conversion and Its Use as a Geothermometer. *Clays and Clay Minerals* **1993**, *41*, 162–177.

- International Atomic Energy Agency. *Geological Disposal of Radioactive Waste: Technological Implications for Retrievability*; IAEA Nuclear Energy Series; NW-T-1.19; International Atomic Energy Agency: Vienna, 2009.
- Jackson, M. L. *Soil Chemical Analysis—Advanced Course*. 2nd ed.; M. L. Jackson: Madison, Wisconsin.
- Kim, J.; Dong, H.; Seabaugh, J.; Newell, S.; Eberl, D. Role of Microbes in the Smectite-to-Illite Reaction. *Science* **2004**, *303*, 830–832.
- Kim, J.; Dong, H.; Yang, K.; Park, H.; Elliott, W. C.; Spivack, A.; Koo, T.; Kim, G.; Morono, Y.; Henkel, S.; et al. Naturally Occuring, Microbially Induced Smectite-to-Illite Reaction. *Geology* **2019**.
- Kozai, N.; Yamasaki, S.; Ohnuki, T. Application of Simplified Desorption Method to Study on Sorption of Americium(III) on Bentonite. *Journal of Radioanalytical and Nuclear Chemistry* **2014**, *299*, 1571–1579.
- Kumar, S.; Pente, A.; Kaushik, C.; Tomar, B. Americium sorption on smectite-rich natural clay from granitic ground water. *Applied Geochemistry* **2013**, *35*, 28-34.
- Kwong-Moses, D. S. Sorption of ¹³⁷Cs onto Weathered Micaceous Minerals from Georgia Kaolin Deposits. Georgia State University 2017.
- Leng, Y.; Henderson, M.; Courtois, J.; Li, H.; Xiong, K.; Tuo, X.; Yan, M. Sorption of Plutonium on Geological Materials Associated with a Chinese Radioactive Waste Repository: Influence of pH. *Journal of Radioanalytical and Nuclear Chemistry* **2016**, *308*, 895–903.
- Li, P.; Liu, Z.; Lin, J.; Ma, F.; Shi, Q.; Guo, Z.; Wu, W. A Method for ²³⁷Np Determination with LSC in the Experiment of Neptunium Sorption onto Bentonite. *J. Radioanal*

- Nucl Chem* **2014**, *299*, 1973–1978. <https://doi.org/10.1007/s10967-014-2960-1>.
- Li, S.; Wang, X.; Huang, Z.; Du, L.; Zhang, D.; Tan, Z.; Wang, X. Sorption-Desorption Hysteresis of Uranium(VI) on/from GMZ Bentonite. *J. Radioanal Nucl Chem* **2016**, *310*, 671–678. <https://doi.org/10.1007/s10967-016-4831-4>.
- Meunier, A.; Velde, B.; Griffault, L. The Reactivity of Bentonites: A Review. An Application to Clay Barrier Stability for Nuclear Waste Storage. *Clay Minerals* **1998**, *33*, 187–196.
- Montgomery, D.; Edayilam, N.; Tharayil, N.; Powell, B.; Martinez, N. The Uptake and Translocation of ^{99}Tc , ^{133}Cs , ^{237}Np , and ^{238}U into *Andropogon Virginicus* with Consideration of Plant Life Stage.
- Moore, D. M.; Reynolds, R. C., Jr. *X-Ray Diffraction and the Identification Analysis of Clay Minerals*, 2nd Ed. Oxford, New York: Oxford University Press, **1997**.
- Ngo, V.; Delalande, M.; Clement, A.; Michau, N.; Fritz, B. Coupled Transport-Reaction Modeling of the Long-Term Interaction between Iron, Bentonite and Callovo-Oxfordian Claystone in Radioactive Waste Confinement Systems. *Applied Clay Science* **2014**, *101*, 430–443.
- Ojovan, M.; Lee, W.; Kalmykov, S. *An Introduction to Nuclear Waste Immobilisation*, 3rd ed.; Elsevier, 2019.
- Oversby, V. M. Important Radionuclides in High Level Nuclear Waste Disposal: Determination Using a Comparison of the EPA and NRC Regulations. Lawrence Livermore National Laboratory 1986.
- Pope, R. Influence of Temperature on Diffusion and Sorption of $^{237}\text{Np(V)}$ through Bentonite Engineered Barriers. Clemson University 2017.

- Powell, B. A., et al. Characterization of radionuclide mobility and speciation during interaction with hydrothermally altered engineered barrier materials and rock. Clemson University. 2016
- Powell, B. A.; Elliott, W. C.; Wampler, J. M.; Kwong-Moses, D. S. Phone Conversation, Oct. 31. Georgia State University. 31 October 2018.
- Pusch, R., 1979, Highly compacted sodium bentonite for isolating rock-deposited radioactive waste: *Nuclear Technology*, v. 45, p. 153-157.
- Pytte, A. The Kinetics of the Smectite to Illite Reaction in Contact Metamorphic Shales. M.A. Thesis, Dartmouth College, New Hampshire, 1982.
- Reynolds, R.; Hower, J. The Nature of Interlayering in Mixed-Layer Illite-Montmorillonites. *Clays and Clay Minerals* **1970**, 18, 25–36.
- Rusco, F. Spent Nuclear Fuel: Legislative, Technical and Societal Changes to Its Transportation. United States Government Accountability Office. 2015.
- Sabodina, M. N.; Kalmykov, S. N.; Sapozhnikov, Y. A.; Zakharova, E. V. Neptunium, Plutonium and ¹³⁷Cs Sorption by Bentonite Clays and Their Speciation in Pore Waters. *Journal of Radioanalytical and Nuclear Chemistry* **2006**, 270 (2), 349–355.
- Schulz, W. *The Chemistry of Americium*; TID-26971; Atlantic Richfield Hanford Company, 1976.
- Sellin, P.; Leupin, O. The Use of Clay as an Engineered Barrier in Radioactive-Waste Management--A Review. *Clays and Clay Minerals* **2013**, 61 (6), 477–498.
- Songsheng, L.; Hua, X.; Mingming, W.; Xiaoping, S.; Qiong, L. Sorption of Eu(III) onto Gaomiaozi Bentonite by Batch Technique as a Function of PH, Ionic Strength, and Humic Acid. *Journal of Radioanalytical and Nuclear Chemistry* **2012**, 292,

889–895.

Środoń, J. Precise identification of illite/smectite interstratifications by X-ray powder diffraction.

Clays and Clay Minerals **1980**, 28, 401-411.

Sternik, D.; Gladysz-Plaska, A.; Grabias, E.; Majdan, M.; Knauer, W. A Thermal, Sorptive and

Spectra Study of HDTMA-Bentonite Loaded with Uranyl Phosphate. *Journal of Thermal Analytical Calorimetry* **2017**, 129, 1277–1289.

Stuckless, J.; O’Leary, D. Geology of the Yucca Mountain Region. U.S. Geological Survey

2007.

Tsai, S.-C.; Ouyang, S.; Hsu, C.-N. Sorption and Diffusion Behavior of Cs and Sr on

Jih-Hsing Bentonite. *Applied Radiation and Isotopes* **2001**, 54, 209–215.

Verma, P.; Romanchuk, A.; Vlasova, I.; Krupskaya, V.; Zakuskin, S.; Sovolev, A.; Egorov,

A.; Mohapatra, P.; Kalmykov, S. Np(V) Uptake by Bentonite Clay: Effect of Accessory Fe Oxides/Hydroxides on Sorption and Speciation. *Applied Geochemistry* **2017**, 78, 74–82.

Villar, M. V.; Martin, P.L.; Barcena, I.; Garcia-Sineriz, J. L.; Gomez-Espina, R.; Lloret, A.

Long-term experimental evidences of saturation of compacted bentonite under repository conditions. *Engineering Geology* **2012**, 149-150, 57-69.

Wampler, J. M.; Krogstad, E.; Elliott, W. C.; Khan, B.; Kaplan, D. Long-Term Selective Retention of Natural Cs and Rb by Highly Weathered Coastal Plain Soils.

Environmental Science and Technology **2012**, 46, 3837–3843.

Winterle, J.; Ofoegbu, G.; Pabalan, R.; Manepally, C.; Mintz, T.; Percy, E.; Smart, K.;

McMurry, J.; Pauline, R. *Geologic Disposal of High-Level Radioactive Waste in Salt*

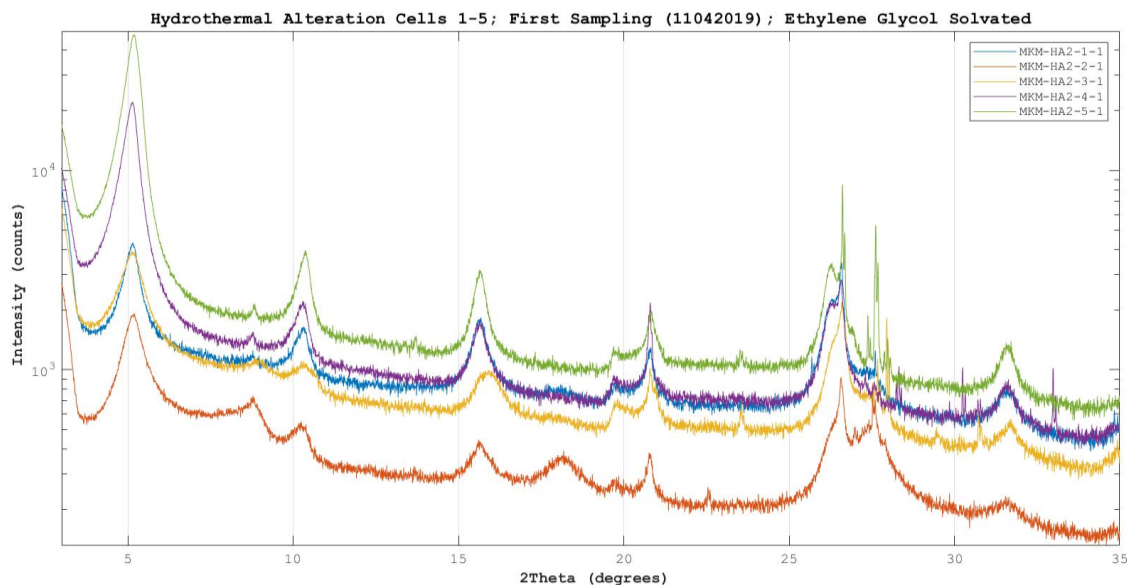
- Formations*; Center for Nuclear Waste Regulatory Analyses: San Antonio, TX, 2012; p 45.
- Xiangke, W.; Wenming, D.; Yingchun, G.; Chanhui, W.; Zuyi, T. Sorption Characteristics of Radioeuropium on Bentonite and Kaolinite. *Journal of Radioanalytical and Nuclear Chemistry* **2001**, 250 (2), 267–270.
- Yates, D.; Rosenberg, P. Formation and Stability of Endmember Illite: I. Solution Equilibration Experiments at 100-250 C and Pv, Soln. *Geochimica et Cosmochimica Acta* **1996**, 60 (11), 1873–1883.
- Zaunbrecher, L.; Cygan, R.; Elliott, W. C. Molecular Models of Cesium and Rubidium Adsorption onto Weathered Micaceous Materials. *Journal of Physical Chemistry A* **2015**, 119, 5691–5700.
- Zavarin, M.; Powell, B.; Bourbin, M.; Zhao, P.; Kersting, A. Np(V) and Pu(V) Ion Exchange and Surface-Mediated Reduction Mechanisms on Montmorillonite. *Environmental Science and Technology* **2012**, 46, 2692-2698.

APPENDICES

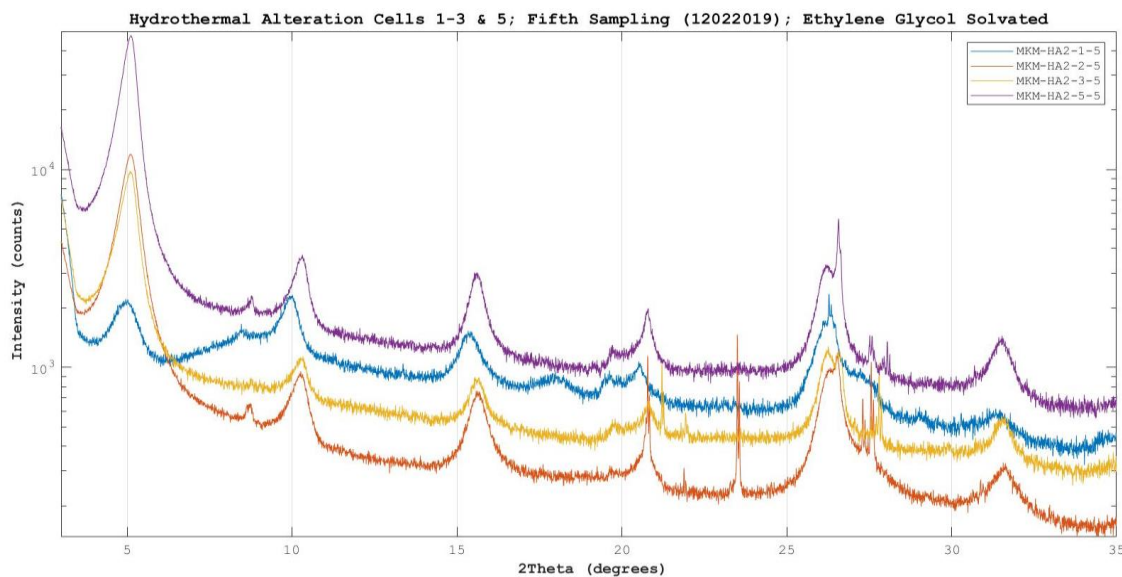
Appendix A

Appendix A.1 X-ray Diffraction Data for Hydrothermal Alteration Experiments

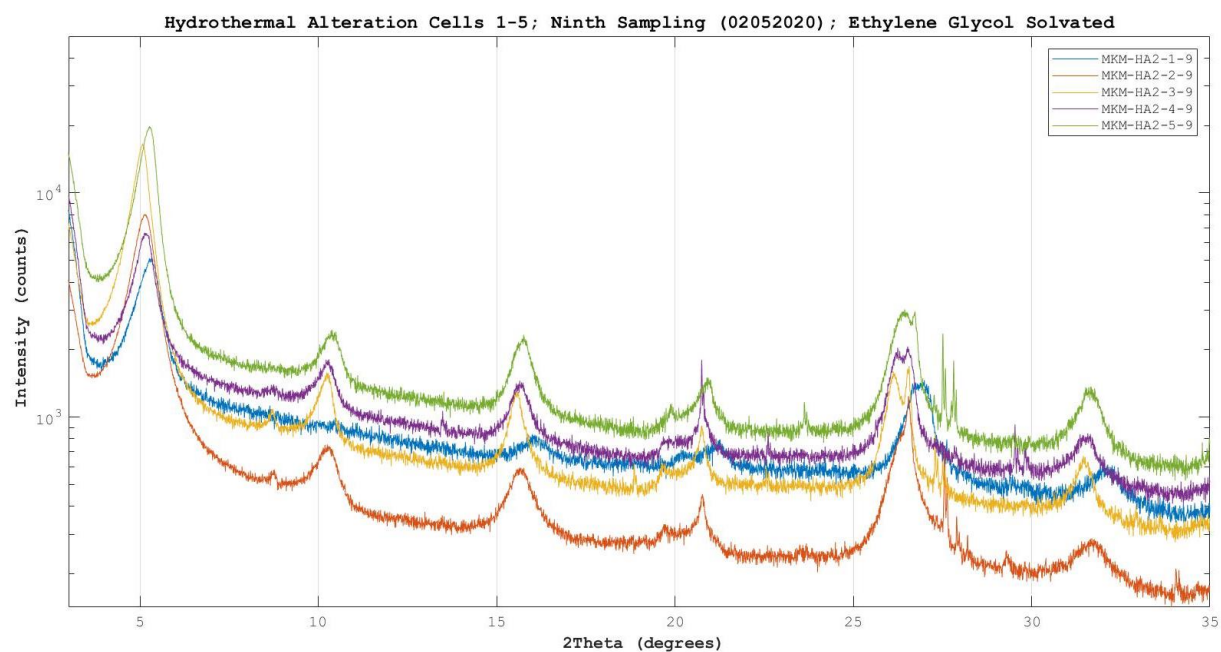
Overlay of Ethylene Glycol-Solvated Diffraction Patterns for the First Sampling (11042019) of Hydrothermal Alteration Experiments



Overlay of Ethylene Glycol-Solvated Diffraction Patterns for the Fifth Sampling (12022019) of Hydrothermal Alteration Experiments



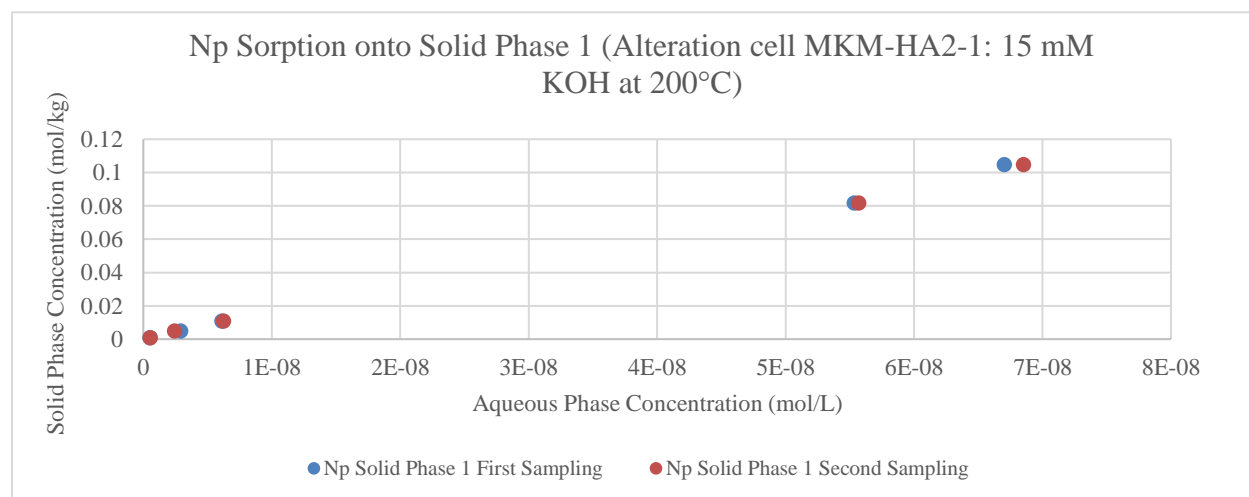
Overlay of Ethylene Glycol-Solvated Diffraction Patterns for the Ninth Sampling (02052020) of Hydrothermal Alteration Experiments



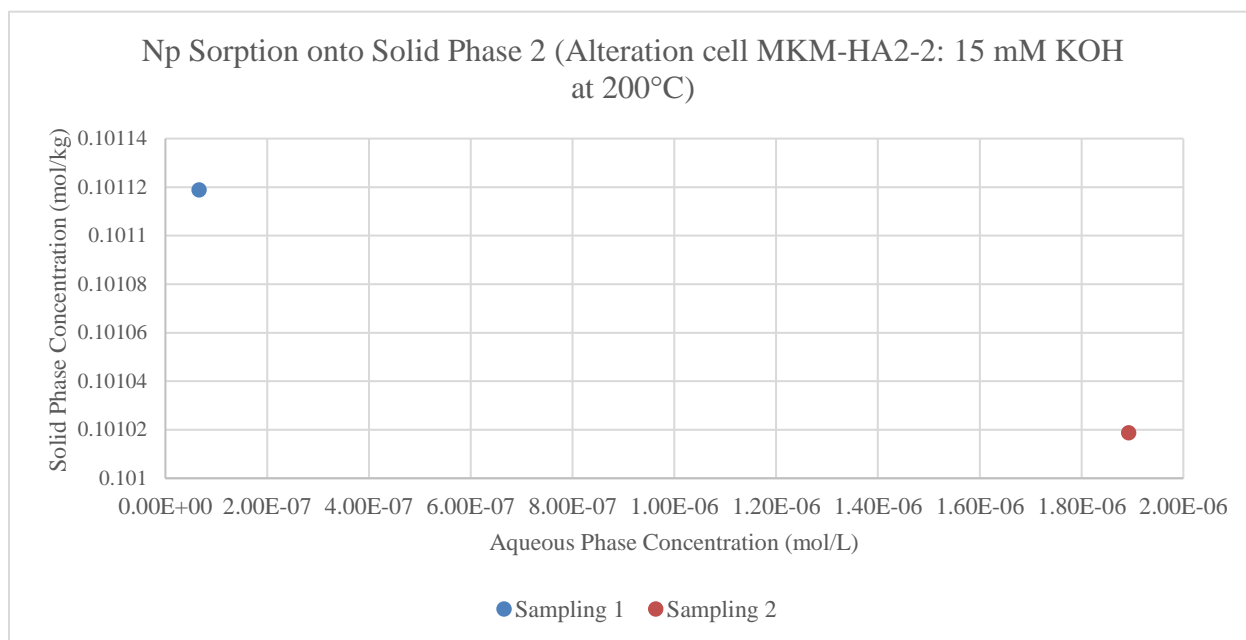
Appendix B

Appendix B.1 Sorption of Np onto Hydrothermal Alteration Products and Unaltered SWy-2 Na-montmorillonite

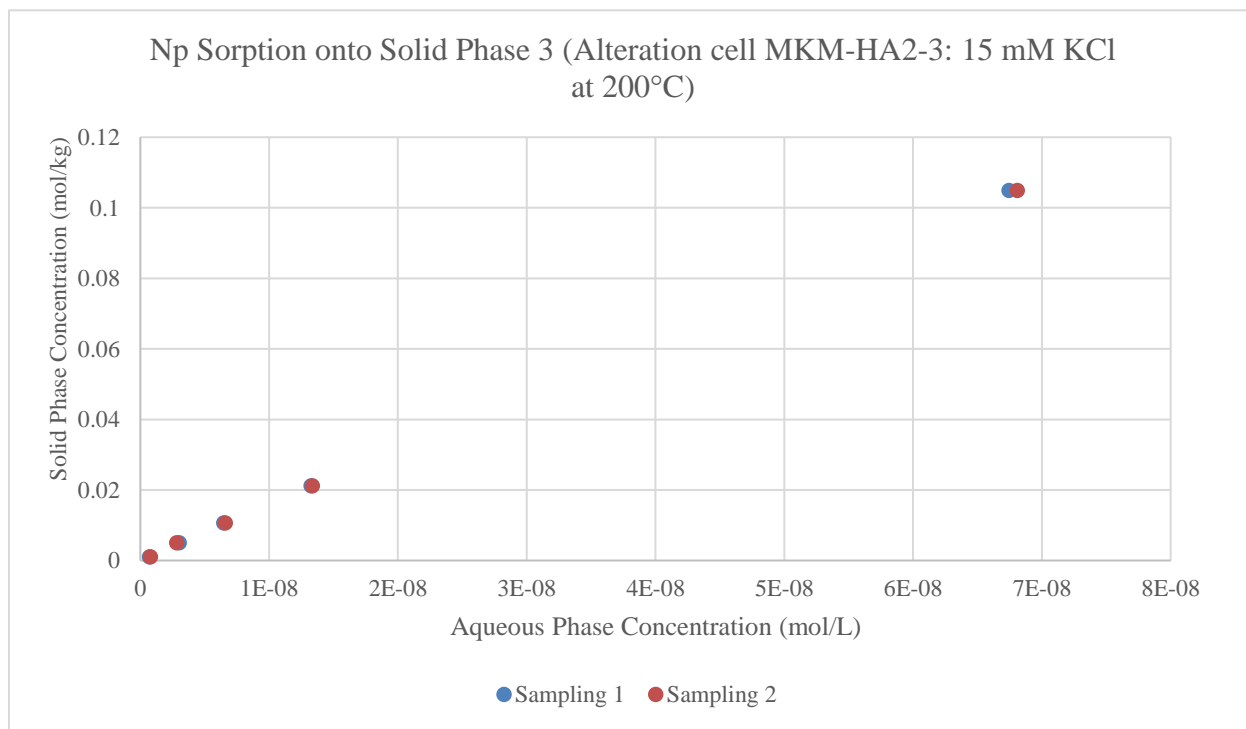
Np Sorption onto Solid Phase 1 (Alteration Cell MKM-HA2-1: 15 mM KOH at 200°C)



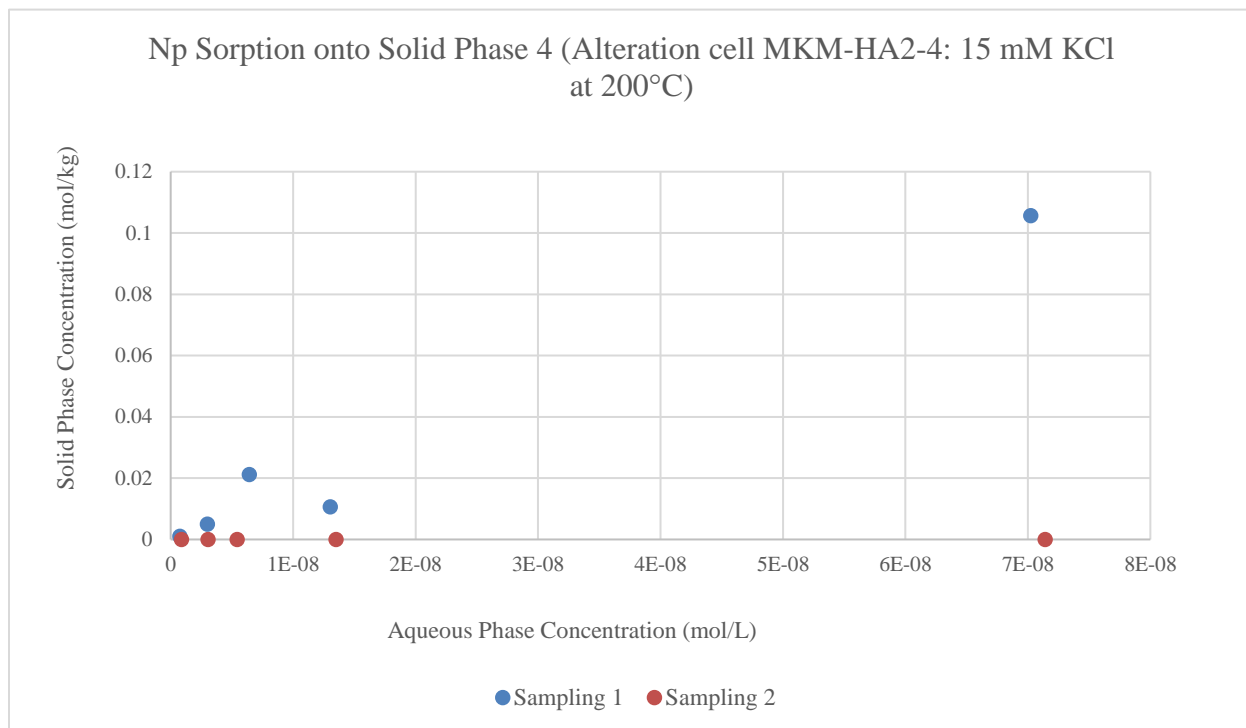
Np Sorption onto Solid Phase 2 (Alteration Cell MKM-HA2-2: 15 mM KOH at 200°C)



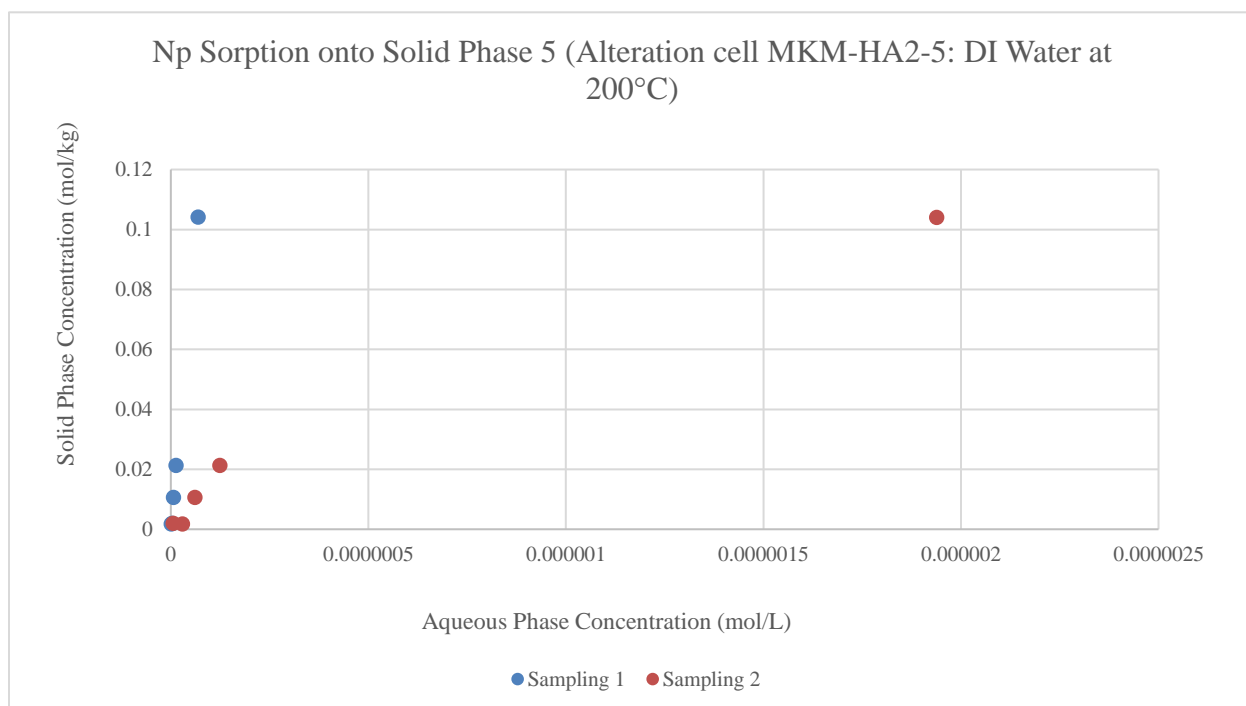
Np Sorption onto Solid Phase 3 (Alteration Cell MKM-HA2-3: 15 mM KCl at 200°C)



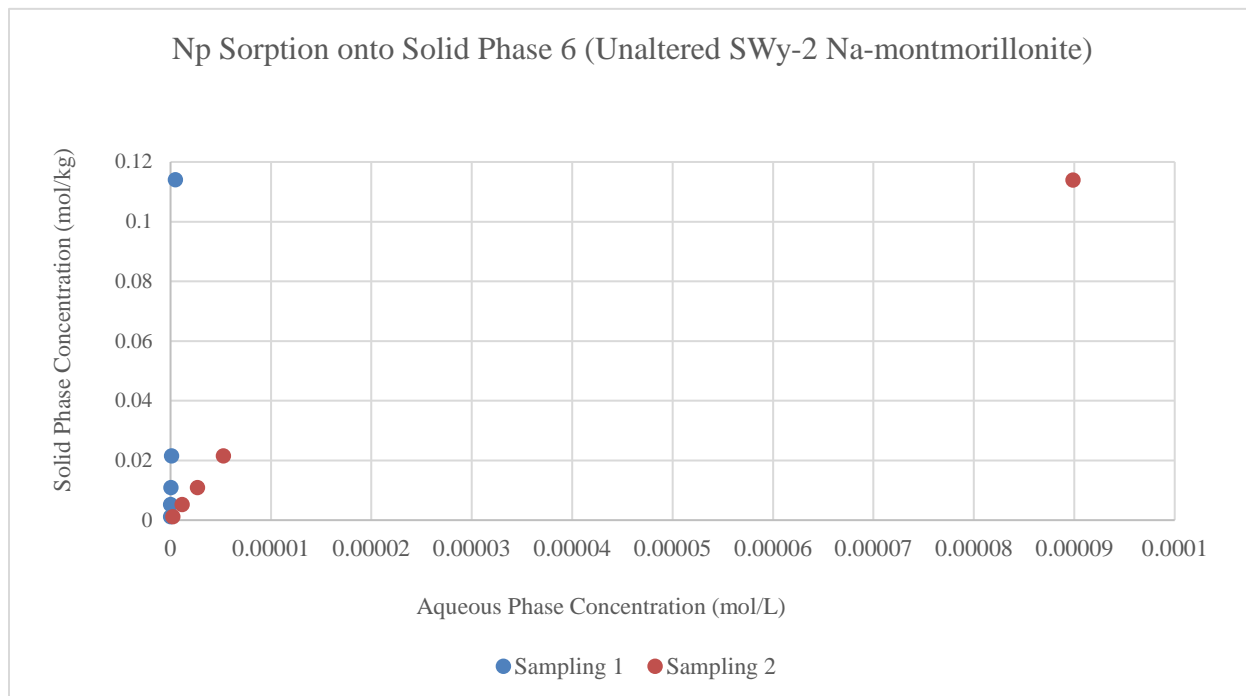
Np Sorption onto Solid Phase 4 (Alteration Cell MKM-HA2-4: 15 mM KCl at 200°C)



Np Sorption onto Solid Phase 5 (Alteration Cell MKM-HA2-5: DI H₂O at 200°C)

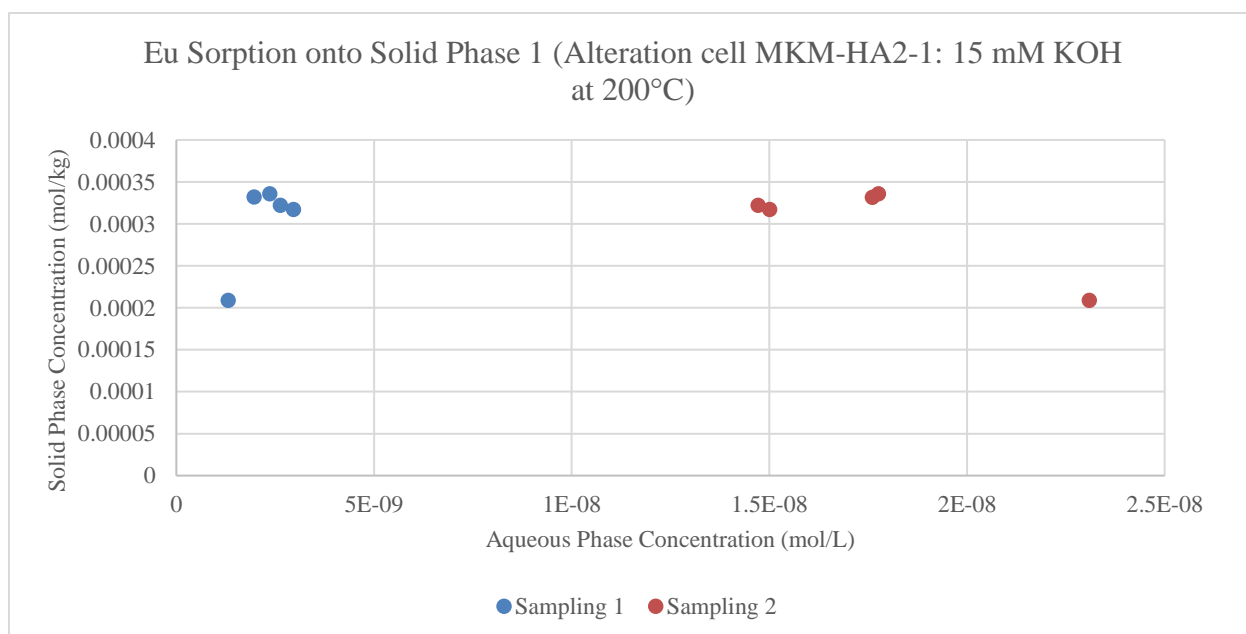


Np Sorption onto Solid Phase 6 (Unaltered SWy-2 Na-montmorillonite)

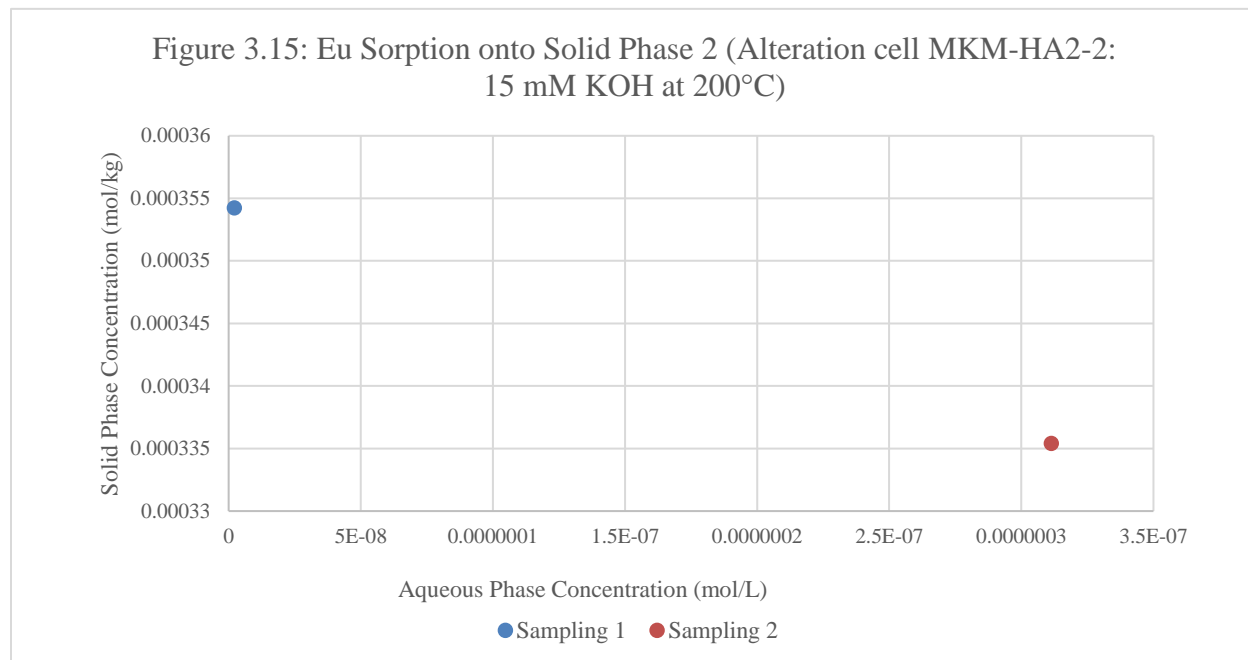


Appendix B.2 Sorption of Eu onto Hydrothermal Alteration Products and Unaltered SWy-Na montmorillonite

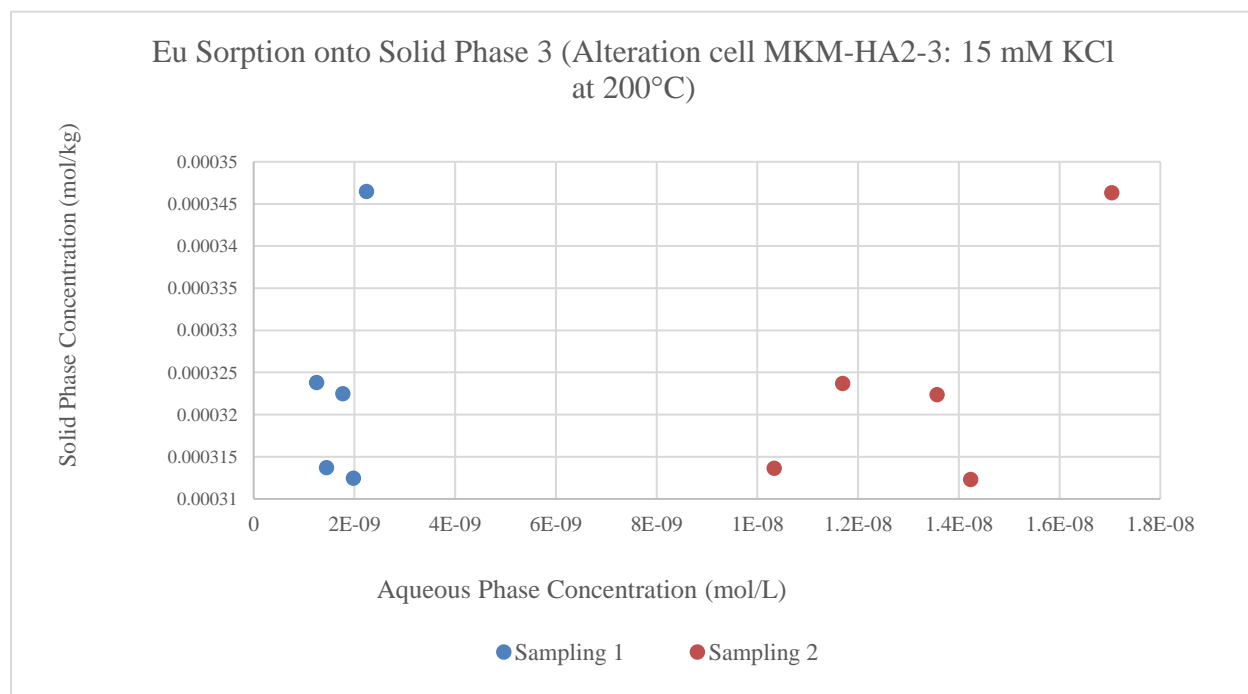
Eu Sorption onto Solid Phase 1 (Alteration Cell MKM-HA2-1: 15 mM KOH at 200°C)



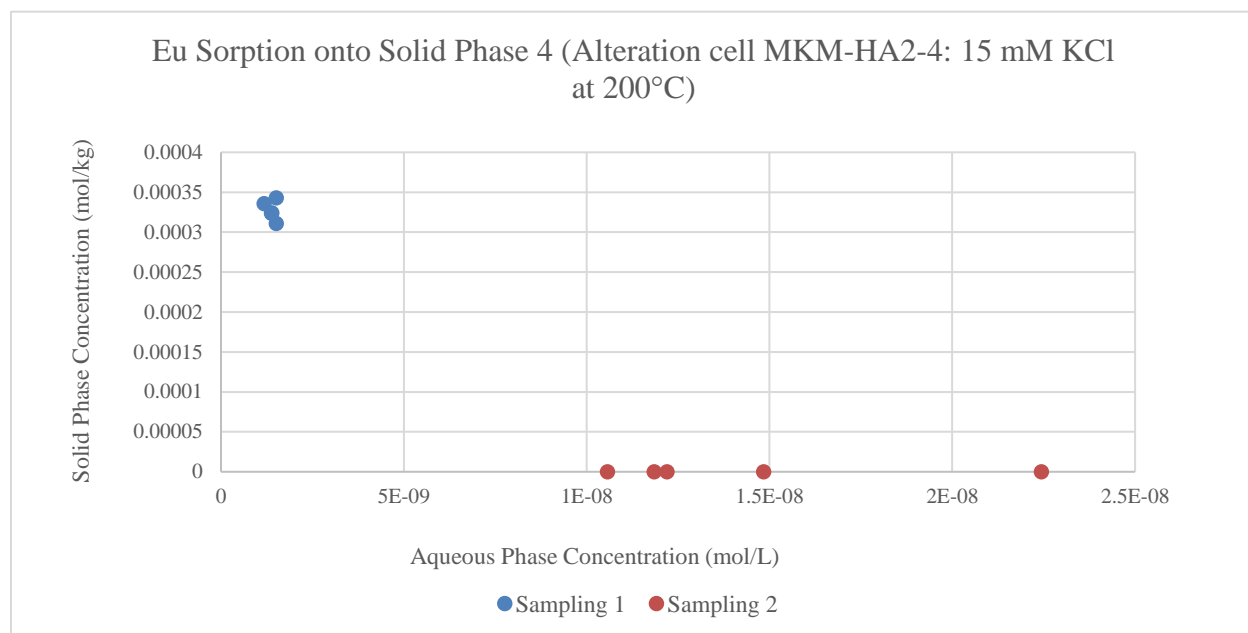
Eu Sorption onto Solid Phase 2 (Alteration Cell MKM-HA2-2: 15 mM KOH at 200°C)



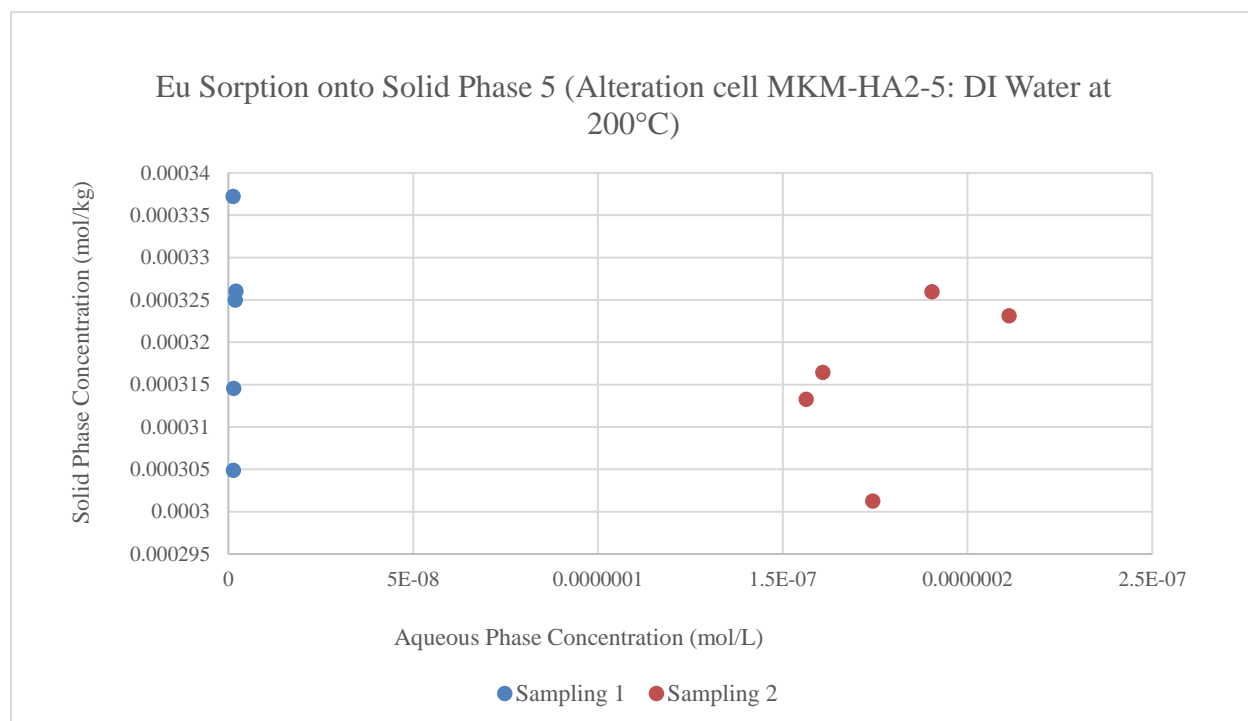
Eu Sorption onto Solid Phase 3 (Alteration Cell MKM-HA2-3: 15 mM KCl at 200°C)



Eu Sorption onto Solid Phase 4 (Alteration Cell MKM-HA2-4: 15 mM KCl at 200°C)



Eu Sorption onto Solid Phase 5 (Alteration Cell MKM-HA2-5: DI H₂O at 200°C)



Eu Sorption onto Solid Phase 6 (Unaltered CMS SWy-2 Na-montmorillonite)